UNIVERSITÀ
DEGLI STUDI
DI PADOVA

UNIVERSITÀ DEGLI STUDI DI PADOVA

Dipartimento di Fisica e Astronomia "Galileo Galilei"

Master Degree in Physics

Final Dissertation

Real-time modelling of DTT plasma scenarios using the RAPTOR transport simulator code

Thesis supervisor
Prof. Piron Lidia
Thesis co-supervisor
Dott. Piron Chiara

Candidate
Pilieci Marco

Academic Year 2023/2024

To my family, as they provided the pedestal upon which I now stand
To the old friends, as their perfect resonance with me will always warm my heart
To those I met along the way, as they ignited anew my love for the World
To those that entrusted me with this work, as they were my essential external driver

I burn my life to make a sunrise that I know I'll never see

Abstract

Controlled nuclear fusion is a promising solution to our current energy crisis that aims to provide clean energy without greenhouse gas emissions or long lasting highly radioactive waste production. Several projects are currently in development to obtain the knowledge necessary to build a commercially viable fusion power plant in the next decades, first and foremost the ITER reactor in construction in Cadarache (France) that will in turn pave the way for the following DEMO reactor, the first hopefully capable of net production of electrical energy. Despite the ambitious aims of ITER, it will not be able to fully explore several key physical and engineering aspects required for the subsequent generation of reactors.

Among these of great importance is the design of their divertors: these devices are able to open the flux surfaces of the containment magnetic field in the reactor and by doing so redirect the flux of particles coming from the plasma toward suitable targets. Among the several advantages of this configuration is that the interaction between the plasma and the chamber wall is kept in a region separated from the core plasma, greatly reducing the influx of impurities, and that the power exhaust is directed toward a specific section of the wall that can thus be the only one designed to sustain extremely high energy fluxes. Despite their importance, ITER will not implement a divertor design suitable for the later DEMO and this brought forth the necessity for a dedicated experiment to study the viability of various divertor configurations in more demanding conditions. This experiment will be DTT (Divertor Tokamak Test), currently under construction at the ENEA Research Center in Frascati (Italy).

To control the plasma dynamics, DTT will make use of an integrated approach that requires a faster-than-real-time physical modeling of the plasma, of which one key component is the simulation of transport phenomena and the corresponding radially dependent physical profiles of the plasma. This will be performed by a 1-dimensional simulator code optimized for control problems and rapid iteration called RAPTOR (RApid Plasma Transport simulatOR). The aim of this thesis is to validate RAPTOR in this application by simulating different plasma scenarios of DTT, following a full time evolution and with both low magnetic field and low externally injected power, as is expected to operate during its first years after commissioning, and with a full suite of external heating systems and higher fields that will be needed for the full scale test of DEMO-like divertor conditions. To improve the results and check their validity, our simu-

lations have been confronted with those obtained with other codes, more specifically METIS, another fast transport simulation code, and ASTRA, a much more complex and computationally demanding simulator. RAPTOR also provides modeling of sawtooth instabilities, an important phenomena that results in periodic crashes of the core temperature of the plasma, caused by topological effects that trigger sudden changes of resistivity in the plasma. Characterizing these sawteeth and how their onset and period are affected by changes in the external heating is useful for controlling them and avoiding negative effects linked to the onset of other types of more problematic instabilities. A double sawtooth sweeping experiment, involving the variation of the radial deposition depth of the external sweeping system while monitoring the sawteeth's period, has been successfully simulated using RAPTOR, showing the robustness of its modelling of this kind of instability.

RAPTOR has thus being tested in different ways in its ability to simulate scenarios that more closely model the actual operation conditions of DTT, paving the way for its future use both for integrated control of the experiment and for obtaining quick preliminary modeling results without using more time consuming codes.

Contents

1 Introduction **1**
- 1.1 The quest for nuclear fusion . . . 1
- 1.2 Tokamak overview . . . 5
  - 1.2.1 Magnetic geometry and confinement . . . 5
  - 1.2.2 External heating systems . . . 7
  - 1.2.3 Blanket . . . 9
  - 1.2.4 Divertors . . . 9
  - 1.2.5 Sawtooth instabilities . . . 11
  - 1.2.6 Other plasma instabilities . . . 12
- 1.3 The DTT project . . . 13
  - 1.3.1 Divertor and Alternative Scenarios . . . 14
  - 1.3.2 Magnetic Systems . . . 16
  - 1.3.3 Heating and Current Drive . . . 16
  - 1.3.4 Diagnostics and Control . . . 18
- 1.4 Outline of this thesis . . . 19

2 The plasma profile dynamics simulation problem and the RAPTOR code **21**
- 2.1 The 1.5D model . . . 21
- 2.2 Flux functions and the Grad-Shafranov equation . . . 22
- 2.3 Diffusion and transport phenomena . . . 25
- 2.4 The RAPTOR code physics model . . . 27

3 Simulation data sets **33**
- 3.1 Simulation of scenario A and comparison with the results obtained with ASTRA 33
  - 3.1.1 Scenario A description and inputs . . . 33
  - 3.1.2 The ASTRA modelling tool . . . 35
  - 3.1.3 Results . . . 36
- 3.2 Simulation of scenario E and comparison with the results obtained with METIS 39
  - 3.2.1 Scenario E description and inputs . . . 39

3.2.2 The METIS modelling tool 41
3.2.3 Results 43

4 Sawtooth control **49**
4.1 Double sweeping test 49
4.2 Effects of sweeping time 54

5 Conclusions **57**

Bibliography **61**

List of Figures

1.1 Cutaway view of the future ITER tokamak fusion reactor. Note the orange human figure below the plasma chamber for scale. Image taken from [ITER] . . . 2

1.2 Schematic representation of a tokamak reactor. **1)** Central Solenoid (CS) coils **2)** Toroidal induced current **3)** Toroidal Field (TF) coils **4)** Toroidal component of the magnetic field **5)** Poloidal Field (PF) coils **6)** Poloidal component of the magnetic field **7)** Total magnetic field. Image modified from original taken from [Li+14]. 6

1.3 Schematic of the magnetic configurations of a tokamak reactor with a divertor. Both the divertor region and the SOL near other portions of the wall are shown in detail. Image taken from [Fed+01] 10

1.4 Schematic representation of the magnetic surfaces during a sawtooth crash according to the Kadomtsev full reconnection model. **i)** Surfaces of equal helical flux before reconnection **ii)** displacement of the hot core and formation of the X-point with subsequent reconnection **iii)** deformation of the magnetic island and expulsion of the hot core **iv)** new cylindrical geometry obtained. Image taken from [Cha10]. 12

1.5 Cutaway render of the future DTT reactor. Courtesy of Divertor Tokamak Test (DTT) facility [DTT]. 13

1.6 Some of the alternative magnetic configurations that can be studied by DTT. Image taken from [Mar+19]. 15

1.7 Poloidal section of the initial configuration of the DTT magnet system (left) and detail of the divertor region (right). 17

2.1 The toroidal coordinate system we will use to describe an axisymmetric plasma. Image taken from [Fel11] 22

3.1 Plasma current and particle density at $\hat{\rho} = 0$ (equal for ions and electrons) used by ASTRA. These values (along with the full radially dependant density profile) have been used as inputs for RAPTOR. The beginning of the flat top is highlighted. 34

3.2 Ions and electrons numerical density profiles in function of $\hat{\rho}$ at $t = 4$ s (dashed line) and at $t = 10$ s (continuous line) used by ASTRA and given as input to RAPTOR. Both these profiles are the results of a linear interpolation between two pairs of instants in the ASTRA time grid, between $t = 3.80$ s and $t = 4.55$ s for the dashed line and between $t = 9.80$ s and $t = 10.55$ s for the continuous line. 34

3.3 Total power injected by the ECRH system in function of time for the scenario A simulation. The beginning of the flat top is highlighted. 35

3.4 Ions and electrons temperature at $\hat{\rho} = 0$ for the simulations of scenario A done with RAPTOR (continuous line) and ASTRA (dashed line). The beginning of the flat top is highlighted. 36

3.5 Ions and electrons temperature profiles in function of $\hat{\rho}$ at $t = 10$ s for the simulations of scenario A done with RAPTOR (continuous line) and ASTRA (dashed line). 37

3.6 Normalized standard deviation between the temperatures computed by RAPTOR and ASTRA in the simulation of the scenario A. The beginning of the flat top is highlighted. 38

3.7 Values of the safety factor q at $\hat{\rho} = 0$ and $\hat{\rho} = 0.95$ for the simulations of scenario A done with RAPTOR (continuous line) and ASTRA (dashed line). The beginning of the flat top is highlighted. 38

3.8 Radial profile of the safety factor at different instants during the simulation of the scenario A obtained with RAPTOR. 39

3.9 Plasma current and particle density at $\hat{\rho} = 0$ for ions and electrons used by METIS. These values (along with the full radially dependant density profile) have been used as inputs for RAPTOR. Both the beginning and end of the flat top are highlighted. 40

3.10 Ions and electrons numerical density profiles in function of $\hat{\rho}$ at $t = 8.00$ s (dashed line) and at $t = 30.01$ s (continuous line) used by METIS and given as input to RAPTOR. Both these profiles are the results of a linear interpolation between two pairs of instants in the METIS time grid, between $t = 7.9515$ s and $t = 8.3655$ s for the dashed line and between $t = 29.8922$ s and $t = 30.3062$ s for the continuous line. 41

3.11 Total power injected by the external heating systems (red) in function of time for the scenario E simulation. The maximum of deposition for the ECRH and ICRH is also shown (blue). Both the beginning and end of the flat top are highlighted. 42

3.12 Ions and electrons temperature at $\hat{\rho} = 0$ for the simulations of scenario E done with RAPTOR (continuous line) and METIS (dashed line). Both the beginning and end of the flat top are highlighted. 43

3.13 Ions and electrons temperature profiles in function of $\hat{\rho}$ at $t = 30.01$ s for the simulations of scenario E done with RAPTOR (continuous line) and METIS (dashed line). 44

3.14 Normalized standard deviation between the temperatures computed by RAPTOR and METIS in the simulation of the scenario E. The beginning and end of the flat top are highlighted. 45

3.15 Values of the safety factor q at $\hat{\rho} = 0$ and $\hat{\rho} = 0.95$ for the simulations of scenario E done with RAPTOR (continuous line) and METIS (dashed line). Both the beginning and end of the flat top are highlighted. 45

3.16 Radial profiles of the safety factor q and the magnetic shear s at $t_1 = 41.38$ s (dashed line) and at $t_2 = 41.41$ s (solid line) from the simulations of scenario E done with RAPTOR. A sawtooth crash has been triggered between the two instants. The horizontal line serve to highlight the $q = 1$ surface (red) and $s = 0.2$ point (blue). 46

3.17 Radial profiles of the temperature of ions and electrons at $t_1 = 41.38$ s (dashed line) and at $t_2 = 41.41$ s (solid line) from the simulations of scenario E done with RAPTOR. A sawtooth crash has been triggered between the two instants. . 47

4.1 Sawtooth sweeping test performed on the scenario E by modifying the radial deposition depth of the ECRH system. The sawtooth period is shown for two tests, one performed by moving varying $\hat{\rho}_{\text{dep}}$ from 0.2 to 0.8 and the other vice-versa. 50

4.2 Radial profiles of parallel current density for the forward (solid line) and backward (dashed line) sweeping test. In both cases three profiles are shown, corresponding to the moments when we had the maximum sawtooth period in the forward and backward sweep and the average between the two. 51

4.3 Example of stabilization of sawteeth using the ECRH. The graph shows the core temperature evolution of a simulation of the scenario E, with the difference that between $t = 32$ s and $t = 52$ s (marked by dashed black lines), the deposition depth has been changed to $\hat{\rho}_{\text{dep}} = 0.5320$. 52

4.4 Sawtooth period in function of $\hat{\rho}_{\text{dep}}$ for simulations of the scenario E. The deposition depth has been maintained at that specific values between $t = 32$ s and $t = 52$ s. The periods are averages that consider only crashes happening after the sawtooth regime stabilized. 52

4.5 Values of the safety factor q at $\hat{\rho} = 0$ and $\hat{\rho} = 0.95$ for the simulations of scenario E done without sawtooth module. Both the beginning and end of the flat top are highlighted as well as the value $q = 1$. 53
4.6 Evolution of the $q = 1$ surface position over time. The results come from a simulation of the scenario E where the sawtooth module has been deactivated. The end of FT is highlighted. 54
4.7 Sweeping tests performed with different possible sweeping times. The sawtooth period is shown in function of the deposition depth. All the tests have been performed with equal initial time $t = 32$ s and varying end time. Gaussian fits of each peak are also shown (dashed lines). 55

Chapter 1

Introduction

1.1 The quest for nuclear fusion

One of the greatest challenges we have to face as a society is the clash between our need for cheap and abundant energy to fuel our civilization and the looming threat of anthropogenic climate change. Up to this point two families of solutions have been implemented with reasonable success, but both with their share of critical issues: the first is renewable energies, like solar, wind and hydroelectric, that have the disadvantage of an aleatory output and can't be readily used for baseline production. The second is nuclear fission, that besides a general distrust from the public presents a still open question of the disposal of highly radioactive wastes.

Another possible solution long sought for is to take inspiration from the principal provider of energy to our planet and harness the power of nuclear fusion, the process that fuels the Sun. It entails two light nuclei merging to create an heavier one and in the process releasing a considerable amount of energy following the formula $E = m\,c^2$ where in this case m is the mass difference between the first and final nuclei. The main challenge in achieving this is the strong Coulomb repulsion between the nuclei that requires extremely high speeds, and thus temperatures, to get close enough so that the attractive nuclear force becomes dominant. With temperatures of the order of 10^8 K needed, the nuclear fuel will fully ionize and become plasma, the so called fourth state of matter and the constituent of stars and most interstellar matter.

Given its nature as a collection of charged particles, plasma can shield electric fields inside of it but is profoundly affected by magnetic fields, thus following the laws of magneto-hydrodynamics. This fact is being exploited to make the construction of a fusion reactor feasible from an engineering standpoint: there is no material capable of resisting the enormous temperatures needed in the fusion plasma, so a magnetic field is used to contain it and keep it away from the walls of the reactor chamber. The charged particles inside the plasma will indeed follow a corkscrew trajectory around magnetic field lines due to Lorentz force, so if the magnetic lines are made to remain inside the reactor chamber without ever crossing its wall the plasma will

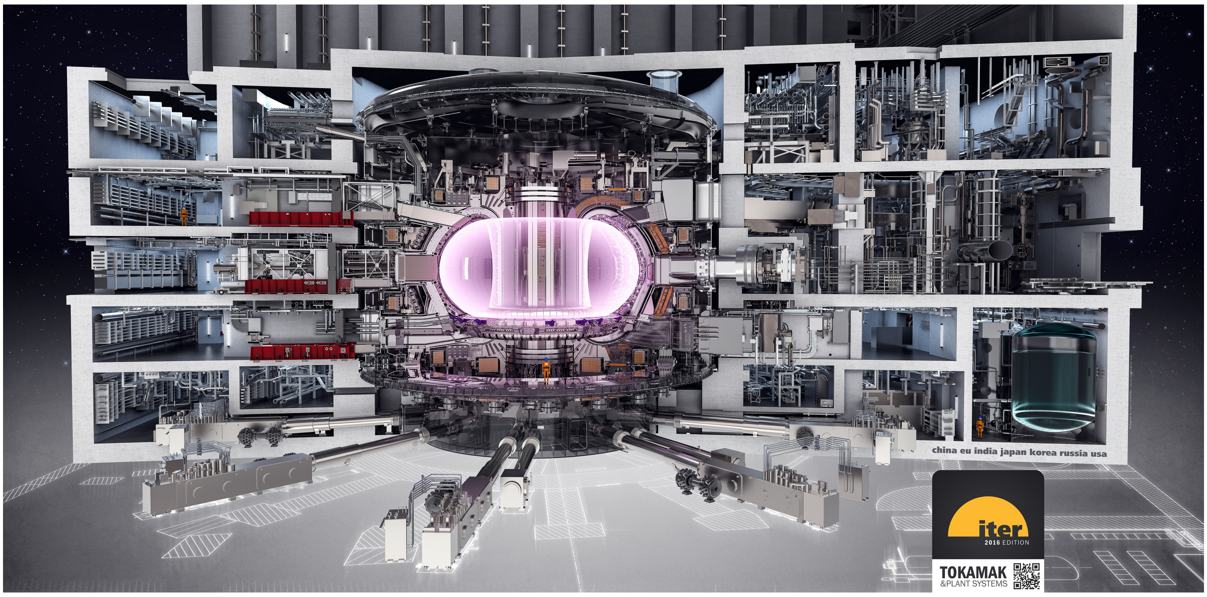

Figure 1.1: Cutaway view of the future ITER tokamak fusion reactor. Note the orange human figure below the plasma chamber for scale. Image taken from [ITER]

remain confined far from any solid object.

Going beyond this simplified view, building a reactor capable of containing a sufficient volume of plasma in an adequate way and with a sufficiently high efficiency as to utilize less energy than what is produced by the nuclear reactions inside it has proven to be an insurmountable technical challenge. Despite extensive research since the first half of the last century, we are still far from a usable commercial reactor, but for the first time this goal seems to be within reach thanks to the **ITER** (Latin for "*the way*") project. Born towards the end of the Cold War, during the 1985 Geneva Summit, ITER has grown to be one of the biggest scientific projects ever undertaken, with the participation of the nations of the European Union, the People's Republic of China, the Republic of India, Japan, the Russian Federation, the Republic of Korea and the United States of America, with a budget of the order of tens of billions of dollars. [1]

ITER will have a toroidal chamber with a major radius of more than 6 meters, with a magnetic field of 5.3 T in the so called tokamak configuration and with a plasma temperature of 150 millions of degrees [Wes11]. A render of the reactor is shown in figure 1.1. To understand the need of a project of such scale, let's first review what goals must be achieved for commercial energy production. The first step is choosing a suitable nuclear reaction. The one that will be used in ITER will be deuterium-tritium fusion:

$$ {}^2_1\mathrm{H} + {}^3_1\mathrm{H} \longrightarrow {}^4_2\mathrm{He} + \mathrm{n} + 17.6\,\mathrm{MeV}. $$

This reaction presents several advantages: deuterium is readily available and there are reasonable means of producing artificially tritium, it has a relatively high reaction Q-value, it reaches a relatively high cross section at the temperatures achievable in a fusion reactor and finally it produces a neutron capable of crossing the confinement field that can be exploited to extract the produced energy from the plasma.[2]

---

[1] The total cost of the project has had various estimates over the years and it's difficult to accurately calculate given the complex international nature of this collaboration.

Having determined the reaction type, the reactor should produce the temperature and density conditions to sustain it in a steady state. The first and most important consideration in obtaining this comes from the study of the energy balance of the plasma. We have

$$\frac{\mathrm{d}W}{\mathrm{d}t} = P_{\mathrm{H}} + P_{\alpha} - P_{\mathrm{L}} - P_{\mathrm{R}},$$

where W is the total energy in the plasma and the terms on the right side of the equation are respectively the power externally injected in the plasma by heating systems, the alpha particle heating power, the power loss due to transport processes and the radiative power loss. A first naive approach could be to ask for a steady state where we have no need to inject external power, relying only on the fusion energy to maintain the temperature of the plasma. In this case, by parameterizing the reactivity of the reaction with a quadratic expression in the temperature and by neglecting radiation losses, after a few mathematical passages we get the condition

$$n\,T\,\tau_E > 3 \cdot 10^{21}\,\mathrm{m}^{-3}\,\mathrm{keV\,s},$$

where the quantity on the left hand side is the **triple product** of density, temperature and of the energy confinement time, that is in turn the characteristic time of decay of the internal energy of the plasma due to only transport losses. A reactor able to respect this condition would reach the so called *ignition*. However this requirement would be extremely difficult to meet and in general it's not needed. In fact, while heating systems add complexity to the device, their presence is desirable as they are an additional and extremely important external mean of control of the plasma. External heaters are also linked to plasma configurations with enhanced confinement. A different criterion could then be to simply ask that the energy exiting the plasma is enough to power these external heaters, once multiplied for a suitable factor η representing the efficiency of electrical power production. This leads to the so called **Lawson's criterion** [Law57]:

$$n\,\tau_E > \frac{12\,T}{\frac{\eta}{1-\eta}\langle\sigma v\rangle E_{\mathrm{f}} - 4\alpha_b T^{\frac{1}{2}}},$$

where $\langle\sigma v\rangle$ is the reaction reactivity, E_{f} is the reaction Q-value and where the radiation losses are approximated as caused only by bremsstrahlung (ignoring line radiation) and are represented by the term that includes the parameter α_b. It's worth noting that this criterion was not developed specifically for magnetically confined fusion, thus all the fusion energy is assumed to exit the plasma. In our practical case instead only the neutron energy escapes.

---

[2] The resulting neutron carries 14.1 MeV of energy while the α carries the remaining 3.5 MeV.

In both cases we can see that the energy confinement time is of the upmost importance in achieving self-sustaining fusion and its optimization is one of the main factors that was taken into account when designing ITER. Its predicted value is usually computed from experimental data taken in a variety of experiments, fitted over several engineering and physical characteristics. The results have the form of a power scaling law of which several form exists. One of the most widely known and upon which the ITER design is based on is the so called ITERH-98P(y,2)[IPEG99], valid for toroidal reactors with a tokamak configuration:

$$\tau_E\,[\mathrm{s}] = 0.0562 \cdot I^{0.93}\, B^{0.15}\, \overline{n}^{0.41}\, P^{-0.69}\, R^{1.97}\, \kappa^{0.78}\, \epsilon^{0.58}\, M^{0.19}$$

where I [MA] is the total plasma current, B [T] is the toroidal magnetic field, $\overline{n}\,[10^{19}\,\mathrm{m}^{-3}]$ is the central line averaged density, P [MW] is the adsorbed power, R [m] is the major radius of the toroid, κ is the *elongation* defined as the ratio between the vertical height of the volume occupied by the plasma (delimited by the last closed flux surface that will be introduced in section 2.3) and the minor radius of the toroid multiplied by two, ϵ is the *aspect ratio*, defined as the ratio between major and minor radius, and M is the hydrogen isotope mass. While they are not included in this case, other parameters are inserted in different power scaling laws, e.g. the cross sectional area of the reactor. Note that this specific law refers to a particular plasma configuration called H-mode that will be discussed in the following sections. In the case of ITER, its design has be chosen so that this equation predicts a containment time greater than 3 seconds.

A final parameter crucial in fixing the requirements needed for a commercial reactor is the ratio between the energy coming from fusion and the external heating required to maintain a steady state. This parameter measures the ability of the reactor to operate as a net energy producer and can be expressed as

$$Q = \frac{\frac{1}{4} n^2 \langle \sigma v \rangle E_{\mathrm{f}} V}{P_{\mathrm{H}}}.$$

where V is the plasma volume and Q is called the **energy gain factor**. The $Q = 1$ condition is called *scientific break-even* and has already been achieved in experiments. This value is however still far from something usable for actual energy production since there are serious losses of efficiency in the extraction of energy from the plasma, in using it to produce electricity and in transforming this electricity into heating power. Moreover, it doesn't account for the power needs of all the other subsystems of the reactor. The target for ITER will be $Q = 10$ but even this will not be enough to commercially produce energy [IAEA02]. Thus, the knowledge obtained by the development and operation of ITER will in turn be used for the construction of an even bigger reactor, called **DEMO**. This will hopefully reach a gain factor high enough to produce more electrical energy than what it consumes, the so called *engineering break-even*, at Q probably around 50.

In the next sections we will now go over the characteristics of a generic fusion reactor with the same design of ITER, then we will concentrate on a specific example called Divertor Tokamak Test (DTT) in construction in Frascati, Italy, explaining its necessity and aims in section 1.3. Then we will describe the needs and strategies to simulate the plasma in one such experiment before concentrating on the specific simulation code that will be used for DTT, called **RAPTOR**[Fel11]. The aim of this work is to use RAPTOR in order to simulate different plasma scenarios of DTT and confront the results with those obtained with other codes as a way to provide a meaningful benchmark and validate its capabilities.

1.2 Tokamak overview

The most promising configuration for a thermonulcear reactor and the one that will be used for both ITER and DEMO is the so called tokamak, from the Russian acronym used to describe these machines (***To****roidal'naya* ***ka****mera s* ***ma****gnitnymi* ***k****atushkami*, toroidal chamber with magnetic coils). First developed in the '50s, it entails a poloidal field confining the plasma coupled with a toroidal field enhancing stability. In this section we will give a quick summary of its components and provide some of the basics on their operation, mostly taking as reference [Wes11].

1.2.1 Magnetic geometry and confinement

The magnetic field of a tokamak is the sum of two components, a toroidal field B_ϕ and a poloidal field $\mathbf{B}_\mathrm{p}$, obtained by different means. The former will be generated by a series of Toroidal Field (TF) coils winded around the plasma. Usual values of the field intensity are above 10 T near the coils themselves and around 5 to 8 T at the center of the plasma, requiring the use of superconducting magnets to achieve the currents needed. While this field is useful to stabilize the plasma, it's not enough to fully contain it. This function is performed by $\mathbf{B}_\mathrm{p}$ that in turn is generated by the toroidal plasma current. This current, of the order of several MA, is mainly induced inside the plasma by the action of the so called Central Solenoid (CS) superconducting coils placed at the center of the toroidal chamber and acting as the primary circuit of a transformer. By forcing a variable magnetic flux in these coils it's possible to induce an electromotive force in the plasma that generates the current. Limitations in the maximum flux achievable are one of the most important limiting factor on the discharge duration in a tokamak and incentivize other methods of current generation, most importantly the bootstrap current generated by neoclassical effects[3] and the current drive given by external heating systems. Finally, a vertically elongated poloidal section presents several advantages, so to control the shape and the position of the plasma a series of Poloidal Field (PF) shape control coils are usually placed around it, giving it

---

[3] In plasma physics, *neoclassical* refers to the description of the plasma that takes into consideration the effects of toroidal geometry on the non-uniformity of magnetic fields.

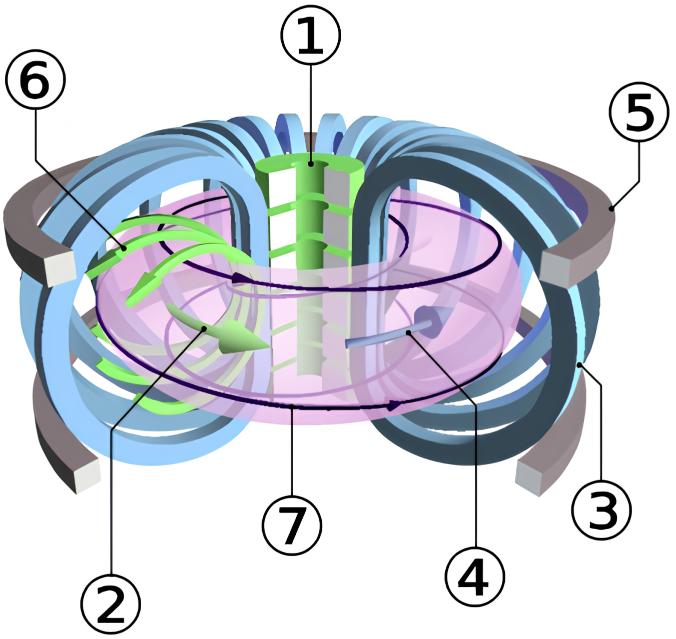

Figure 1.2: Schematic representation of a tokamak reactor. **1)** Central Solenoid (CS) coils **2)** Toroidal induced current **3)** Toroidal Field (TF) coils **4)** Toroidal component of the magnetic field **5)** Poloidal Field (PF) coils **6)** Poloidal component of the magnetic field **7)** Total magnetic field. Image modified from original taken from [Li+14].

a characteristic D-shaped section. A schematic representation of the systems just described is shown in picture 1.2.

The resulting magnetic field has an helical shape that gives it a certain resilience against instabilities. An important and useful parameter to quantify the helicity of the plasma is the so called **safety factor**, indicated by the letter q. Qualitatively, it's the ratio between the number of turns that a field line makes along the toroidal direction for each turn in the poloidal one. More rigorously, we have

$$q = \frac{1}{2\pi} \oint \frac{1}{R} \frac{B_\phi}{B_\mathrm{p}} \mathrm{d}s, \tag{1.1}$$

with the integral carried out over one poloidal circuit. Other possible definitions exists, most notably as the ratio between the rate of change of toroidal and poloidal magnetic fluxes. The derivative of q is called *shear* (s) and is another important parameter to study the plasma profile. It can be defined as

$$s = \frac{r}{q} \frac{\mathrm{d}q}{\mathrm{d}r},$$

with r the minor radius of the torus. The profile of q determines many characteristics of the tokamak operations and allows to classify it in several modes called *plasma scenarios*. The most common is the inductive scenario, where at the plasma center a large surface with $q = 1$ is developed, with a monotonic increase of q when moving toward the plasma edge. This scenario is characterized by a type of instability called *sawtooth instability*, that we will study in more detail later, linked to the aforementioned $q = 1$ surface. Other scenarios are achieved by obtaining a large fraction of current non-inductively, with q greater than one and reverse shear near the core, but are used less commonly given the challenges in reaching these regimes. It's also worth nothing that several other instability are uniquely determined by the profile of q and in particular by the position of the surfaces where it has a rational value, defined as $q = -m/n$ where m and n are the *plasma mode numbers*.

Another useful parameter to measure the efficiency with which the magnetic field is able to confine the plasma is the ratio of the plasma pressure and the magnetic pressure, called β:

$$\beta = \frac{p}{B^2/2\,\mu_0}. \tag{1.2}$$

Several other definition of β exists, most notably the **poloidal** β that takes into consideration only the poloidal component of the magnetic field and integrates p over a poloidal cross section.

An important phenomenon to consider is the so called *High confinement mode* or **H-mode**. in this plasma regime, a *transport barrier* is created at the edge of the plasma, with a rapid pressure and density gradient called *pedestal* that in turn greatly increase the density at the plasma core. The causes of the onset of the H-mode are not completely understood, but it's usually seen in experiments with a significant external heating and is considered of high relevance to reach the conditions needed in future reactors.

1.2.2 External heating systems

As already mentioned, tokamak reactors will make use of external heating systems. Indeed, the majority of the energy generated by fusion escapes the plasma with the neutrons and the conditions to obtain a reaction rate that would allow self-sustainment are prohibitive. One way to heat the plasma is through ohmic heating by exploiting the current generated inside it. While this method can be useful during the plasma startup phase, it's generally inadequate when it reaches its final steady state due to the higher temperature of the particles inside it that reduce their collisional cross section, reducing in turn the plasma resistivity. This makes necessary the use of systems capable of injecting back power inside the plasma, with the additional benefit of acting as powerful external actuator and being able to drive non-inductive current. They are in general called Heating Current Drive (HCD) systems. We will now go through the most common types.

Neutral Beam Injectors The idea behind the Neutral Beam Injector (NBI) is to bombard the plasma with a beam of high velocity neutral particles, capable of crossing the magnetic field, that will deposit inside it both their energy and momentum. The energy of the neutral particles is chosen so that it will be deposited near the plasma core and is usually of the order of the hundreds of keV or more. Given the inherent difficulties in reaching these kind of energy with neutrals, the most common strategy for the production of these beams is to accelerate charged particles and to neutralize them in flight. One possibility is to use positively charged ions passing through a neutralization chamber filled with low density gas. However, the neutralization cross section in these kind of processes is so small that a large portion of the beam will inevitably be wasted. Because of this the use of negative ions is preferred given their much higher neutralization probabilities and despite the significant engineering challenge in producing and accelerating them. Neutral beams can be either be injected perpendicularly to the torus, causing both losses due to the rippling of the magnetic field and the possibility of a fraction of the beam crossing through the plasma and hitting the back wall, or more tangentially, with the added benefit that the transferred momentum will help induce current inside the plasma.

Electron Cyclotron Resonance Heating It is possible to heat the plasma by using electromagnetic waves exploiting resonance absorption, a collision-less phenomenon that is thus suited to heat high temperature plasma. The simplest of these systems is the Electron Cyclotron Resonance Heating (ECRH), working at frequencies around 100-200 GHZ corresponding to the cyclotron frequency of the electrons. The electron cyclotron waves are emitted usually by phased array antennas outside of the plasma that allow both for a fine steering of the wave and, by changing its frequency and remembering that the cyclotron frequency depends on the intensity of the magnetic field, control the deposition depth. ECRH can also be used for current driving. The way this is accomplished is by having waves with high phase velocity that couples with that of the electrons moving in a particular direction and resonating with them. This preferential heating lowers the collisionality of these electrons and with that the resistance they feel, reaching a condition with a so called ’asymmetric resistivity’ that generates current driving.

Ion Cyclotron Resonant Heating Similarly, if instead of the electron cyclotron frequency the ion’s one is used we have the Ion Cyclotron Resonance Heating (ICRH), with frequencies of the order of tens to one hundred MHz. While it can directly and efficiently heat the ions, the main disadvantage of this system is that the wave is evanescent in the vacuum outside the plasma, forcing the antennae to be only centimeters away from the plasma volume with greatly increased engineering complexity.

Lower Hybrid Resonance Heating Finally, frequencies around 1 to 8 GHz are utilized by the Lower Hybrid Resonance Heating (LH) that exploits lower hybrid oscillations that involve both ions and electrons. Given that its resonant frequency depends on the electron density, it’s not possible to precisely control the deposition depths and in general LH have not proven to be particularly suited for heating purposes, while being much more effective as current drivers. On top of the asymmetric resistivity mechanism already mentioned for the ECRH, with LH another important contribution in current driving is given by direct momentum transfer from the wave to the electrons.

1.2.3 Blanket

The wall facing the plasma is mostly covered by a structure called *blanket* that is a crucial component of every reactor. It performs three key roles: the first is protecting the vacuum vessel and other components behind it from the radiative power flux and the high energy neutron radiation coming from the plasma. Second, is housing the coolant pipes that carry away the thermal energy exiting the reactor so that it can be converted into electricity. The final and most complex role in the most advanced designs is to perform tritium breeding, a technology that it's still been developed but that will be paramount for the success of future reactors. As already mentioned, the most promising fuel mixture in fusion reactors is deuterium and tritium. While the former is readily available and can be extracted from seawater, the latter is an unstable isotope with a half life of 12.32 years so it has to be continually produced. Nowadays, it's provided by fission reactors but ideally it would be desirable to make commercial fusion reactors self-sufficient. Given that only one neutron is produced for every tritium atom burned and given losses and inefficiencies in the system, every neutron interacting with the breeding blanket should react more than once. In ITER, the chosen production pathway is through the neutron activation of lithium, more specifically

$$^{7}_{3}\mathrm{Li} + \mathrm{n} \longrightarrow {}^{4}_{2}\mathrm{He} +^{3}_{1}\mathrm{H} + \mathrm{n} \quad \text{and} \quad ^{6}_{3}\mathrm{Li} + \mathrm{n} \longrightarrow {}^{4}_{2}\mathrm{He} +^{3}_{1}\mathrm{H},$$

where the first reaction doesn't consumes the neutron and has the advantage of having a much larger cross section at higher energy, allowing the neutron to catalyze several breakups of $^{7}_{3}\mathrm{Li}$ while it thermalizes before being absorbed by a $^{6}_{3}\mathrm{Li}$.

1.2.4 Divertors

Despite the presence of the magnetic field containment, plasma particles are still able to diffuse from a magnetic field line to the other due to collisions, moving toward the chamber wall. This presents two problems: first, it subjects the walls to high thermal loads, forcing it to be covered in adequate shielding materials. Second, the Plasma-Wall Interaction (PWI) causes a release of impurities with higher atomic numbers that can penetrate in the core plasma and quickly degrade its properties. A possible solution to mitigate the first problem is the use of the so called *limiters*, i.e. protrusion from the wall that intercept the magnetic field lines. This way,

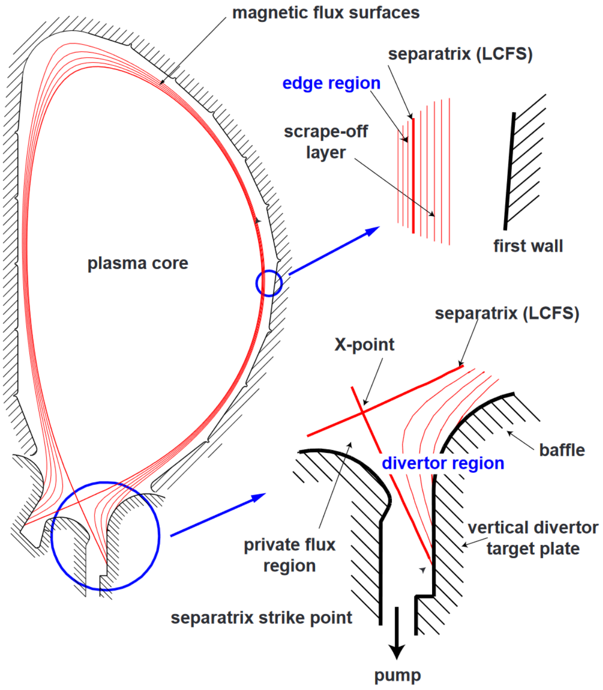
magnetic flux surfaces
separatrix (LCFS)
edge region
scrape-off
layer
first wall
plasma core
separatrix (LCFS)
X-point
baffle
divertor region
vertical divertor
target plate
private flux
region
separatrix strike point
pump

Figure 1.3: Schematic of the magnetic configurations of a tokamak reactor with a divertor. Both the divertor region and the SOL near other portions of the wall are shown in detail. Image taken from [Fed+01]

as the plasma particles move outward they will encounter the limiter first and interact with it before reaching the rest of the wall. This way, only the limiters have to be engineered to sustain the heat loads coming from the plasma. As we will see in the next chapter, it's useful to think of the magnetic field in the plasma as lying on concentric flux surfaces. In this configuration the most external flux surface that still doesn't touch the limiter is called Last Closed Flux Surface (LCFS) while in all those beyond it the plasma density decreases rapidly in a volume called the Scrape Off Layer (SOL). Limiters still don't solve the impurities problem since the PWI still happens next to the LCFS so that heavy ions released by the walls can cross it and enter the plasma core. Moreover, there is no way to control the flux of plasma hitting the limiter in order to spread it on a larger area.

To solve these issues, most modern tokamak instead use a different system called *divertor*. In this case dedicated magnets open the LCFS creating an X-point, with two legs connecting themselves and wrapping around the plasma and two other being diverted towards external targets. A schematic view of a typical set up is shown in picture 1.3 where we can see the typical shape of the LCFS, in this case called *separatrix*. The advantages are evident: the PWIs happens in an area where, beyond the separatrix, there isn't the plasma core but rather a separated volume called *private flux region* that is continuously evacuated by vacuum pumps, so that impurities cannot reach the plasma core and are instead being removed. The divertor also acts as an exhaust for the plasma, allowing a steady exchange of particles and in particular to remove the helium generated by the fusion reaction. Moreover, the magnets in the divertor region can be controlled as to flare the magnetic lines and make them hit the targets at a shallow angle, considerably spreading the heat flux that, in bigger machines, would otherwise be hardly manageable. Over the years divertors have been linked with a considerable increase in performance and containment capabilities, making them a key component of all future reactors.

1.2.5 Sawtooth instabilities

Tokamak plasma is subject to a wide variety of instabilities, with different phenomenology, causes and effects. Before giving a quick rundown of some of the most notable, we will focus on a class of instabilities called **sawtooth crashes** that are of greater interest for this work. Sawtooth instabilities [Cha10] are characterized by an expulsion of hot particles from the core, causing a flattening of the temperature, density and q profiles. They are connected to the onset of the so called $n = m = 1$ *internal kink mode*. Kink modes are MHD oscillations of the plasma with amplitude described as

$$\xi = \exp\left(i\, m\, \theta - i\, n\, \phi\right)$$

where θ and ϕ are the poloidal and toroidal angles, while m and n are the plasma mode numbers we are already mentioned when dealing with the safety factor (section 1.2.1). The $n = m = 1$ kink onset is related to the appearance inside the plasma of a $q = 1$ surface and leads to a tilt and shift of the core plasma. While kink modes are crucial to the onset of sawtooths, their stability is connected also to the presence of fast ions, sheared flows, pressure anisotropy and several other effects. Qualitatively, as the core temperature rises, the temperature profile peaks, allowing the $q = 1$ surface to enter the plasma, triggering the kink instability causing the temperature crash and an increasing of q_0 that returns above one. Then the cycle repeats.

A first attempt to give a comprehensive explanation of the dynamics of the crash is the **Kadomtsev full reconnection model** [Kad75]. According to this model the kink mode causes a displacement of the central core of the plasma and the creation of a magnetic X-point on one side. Subsequently a magnetic island with $m = 1$ starts to grow and makes the surfaces with the same helical flux touch and reconnect, causing the expulsion of the hot core and the formation of a new magnetic equilibrium. A schematic representation of this process is shown in figure 1.4. Further experimental studies have however shown that this model is not accurate, since the reconnection process is interrupted when the magnetic island is still of modest size, q_0 remains below unity after the crash despite Kadomtsev predictions and the predicted reconnection timescale is too slow compared to what is observed. A number of alternative models have been proposed over the years, most notably the so called *partial reconnection model* that entails a different kind of relaxation for the core and magnetic island and the creation of two current sheets that then rapidly diffuse. Later, in section 2 we will give a model to predict the onset of the crash based

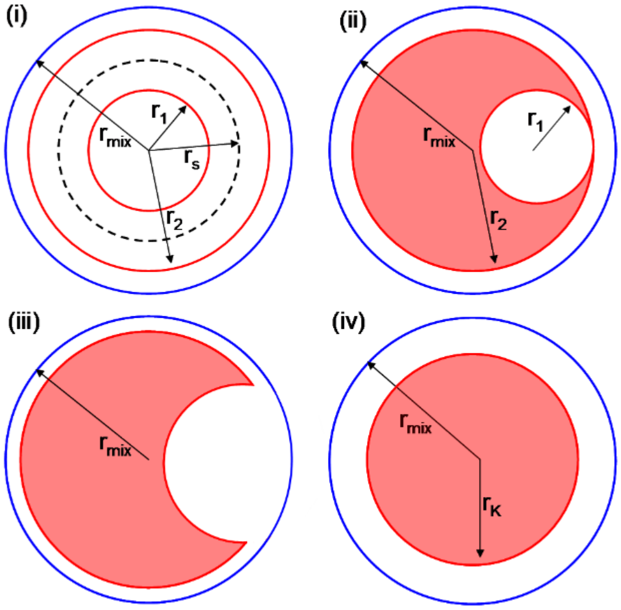

Figure 1.4: Schematic representation of the magnetic surfaces during a sawtooth crash according to the Kadomtsev full reconnection model. **i)** Surfaces of equal helical flux before reconnection **ii)** displacement of the hot core and formation of the X-point with subsequent reconnection **iii)** deformation of the magnetic island and expulsion of the hot core **iv)** new cylindrical geometry obtained. Image taken from [Cha10].

on the calculation of the stability of the $n = m = 1$ kink mode.

Sawtooths can have different effects on the plasma: large sawtooths with longer periods can trigger other instabilities while short period sawtooths can have the beneficial effect of avoiding build up of helium ashes in the plasma core. For these reasons, sawtooth control is of great interest, both in the form of stabilization to completely avoid the crashes, or destabilization to increase their frequency and avoid the onset of worse instabilities. This is usually done by means of the HCD systems that can act on the population of fast ions, current and pressure profiles, electron temperature, plasma rotations and so on, which each of these having a different effect on sawtooth instabilities. In chapter 4 in particular we will see how the sawtooths' period can be modified by RF power deposition near the $q = 1$ surface.

1.2.6 Other plasma instabilities

We will now briefly introduce two other notable plasma instabilities, which have been encountered in this thesis project: the Neoclassical Tearing Mode (NTM) and the Edge Localized Mode (ELM).

Magnetic Islands and Neoclassical Tearing Modes The presence of surfaces inside the plasma where q has rational values can causes MHD instabilities called *tearing modes* that can locally change the magnetic topology. This can manifest itself with reconnection of the magnetic lines and formation of X-points that define a separatrix encompassing an area of the plasma called *magnetic island*. Inside these island there can be a considerable degradation of confinement and reduction of pressure gradients, that in turns might lead to a further destabilizing reduction of the bootstrap current. Tearing modes driven by this mechanism are called *Neoclassical Tearing Modes* and are one of the most deleterious plasma instabilities.

Edge Localized Modes H-mode is characterized by a particular class of instabilities called *Edge Localized Modes*, consisting on a periodic expulsion of material from the edge of the plasma connected to a collapse of the pedestal. They differentiate themselves depending on the severity and period, with faster ELMs (also called *grassy*) linked to considerable degradation of confinement and longer and larger ELMs (called *giant*) extremely dangerous because of the consequent considerable increase in exhaust power on the divertors.

1.3 The DTT project

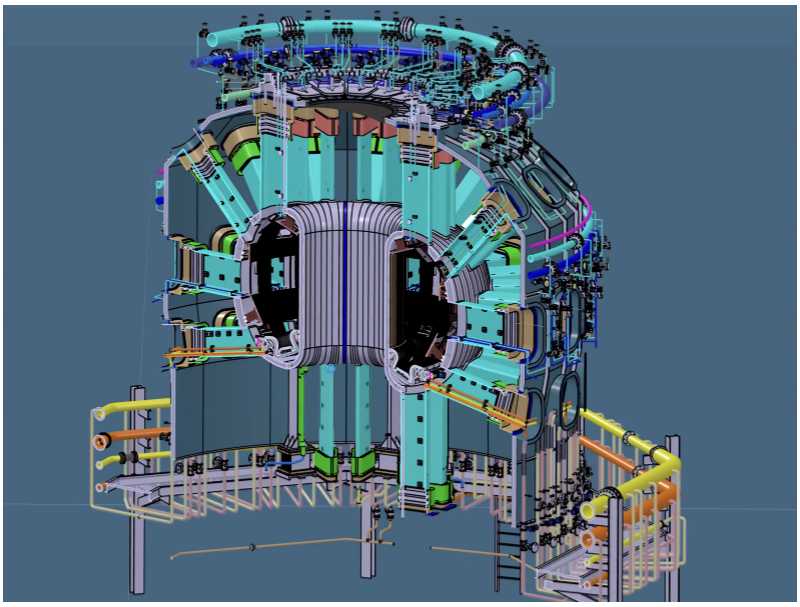

Figure 1.5: Cutaway render of the future DTT reactor. Courtesy of Divertor Tokamak Test (DTT) facility [DTT].

Divertors are one of the key components in the future success of commercial nuclear reactors and the choice of a suitable design will be paramount for the construction of DEMO. However, ITER will utilize a standard approach to power exhaust that might not be usable in future larger

Machine	DTT	ITER
R [m]	2.11	6.2
a [m]	0.64	2.0
R/a	3.3	3.1
V [m^3]	29	837
I_P [MA]	5.5	15
B_ϕ [T]	6	5.3
n_e/n_G	0.42	0.7
q_{95}	3	3
k_{95}	1.65-1.75	1.70-1.85
δ_{95}	0.3	0.33-0.49

Table 1.1: Confront of some physical and technical parameters of DTT [Mar+19] and ITER [IAEA02].

experiments. In order to explore various design possibility it was decided to build a reactor whose main experimental goal will be to test different exhaust schemes called **DTT** (***D**ivertor **T**okamak **T**est Facility*) [Mar+19]. DTT is currently under construction at the ENEA Research Center in Frascati (Italy) under a consortium made of ENEA, CREATE, Eni, Consortium RFX, INFN, *Università degli Studi della Tuscia, Università degli Studi di Milano-Bicocca, Università degli Studi di Roma Tor Vergata, Politecnico di Torino*, CNR and CETMA. Its projected costs is of 614 millions of euros, is expected to begin plasma operations in 2025 and will have an operative life of 25 years, during which it will perform roughly 25000 shots.

The main objectives of DTT will be to asses the viability in terms of power loads as well as magnetic and technological constrains of advanced divertor configurations and other alternative technologies like liquid metal systems, with an emphasis on their possible use on DEMO. It will also experimentally study the science of plasma heat and particle exhaust with parameters beyond those of the current machines. In order to do this, special consideration have been made to the design of the machine, like symmetrized coils and vacuum vessel to allow a double divertor. Despite DTT being scaled down, the relevancy for future designs is guaranteed by choosing the reactor characteristics so that several parameters that determine the physics of the SOL and divertor region will have similar values to those of DEMO. Moreover, the ratio between the power exiting the plasma at the separatrix and the major radius will be around 15 MW/m, similar to the values expected with ITER and DEMO. The main characteristics of DTT are given in table 1.1.

1.3.1 Divertor and Alternative Scenarios

In order to allow for modifications and upgrades, the DTT divertor has been designed so that it can be installed and extracted by a remote handling system. The initial design sees 54 sections (called *cassettes*), each containing an inner and outer target and a dome between them as plasma facing components with a FAST-like design and capable of accommodating different magnetic configurations. These will be made of Tungsten mono-blocks with CuCrZr cooling pipes and are expected to receive thermal loads of the order of $15 \div 20\,\mathrm{MW/m^2}$ while remaining below 1100° C at their surface.

Beside the initial Single-Null (SN) scenario that will be studied in this work, a number of alternative scenarios have been considered. A selection of magnetic configurations that can potentially be studied is shown in figure 1.6. The Double-Null (DN) makes use of a second upper divertor that allows to split the average heat load, at least during the flat top (FT), the state of stationary regime in the middle of a plasma discharge). The Snowflake Divertor (SFD) introduces a second order null point, splitting the separatrix into six legs with two close X-points and lower poloidal field in the divertor region. The X-divertor (XD) increases the poloidal flux expansion thus flaring the flux surfaces. The Super-X Divertor (SXD) further flares the flux surfaces by increasing the major radius of the targets. DTT will be able to achieve this condition with a 4.5 MA plasma and a outward leg length of the separatrix of $\simeq 0.73$ m or with a 3 MA plasma with a reduced plasma volume and modified in-vessel components. A configuration with Negative Triangularity (NT) improves flaring on the inner leg and can be achieved at low current and/or L-mode or, with a modified first wall and divertor, also in H-mode for short periods of time.

A liquid metal system has also been envisioned, making use of a Porous Capillary System (PCS) filled with liquid lithium or tin, with the advantage of having self healing properties and insensitiveness to neutron damage. While this technology has already been tested in tokamak conditions, DTT will be able to subject it for the first time to the harsh environment of an integrated plasma scenario in H-mode with a divertor configuration. DTT can also test a vapour-box configuration to greatly reduce the evaporated metal mass flow to the plasma.

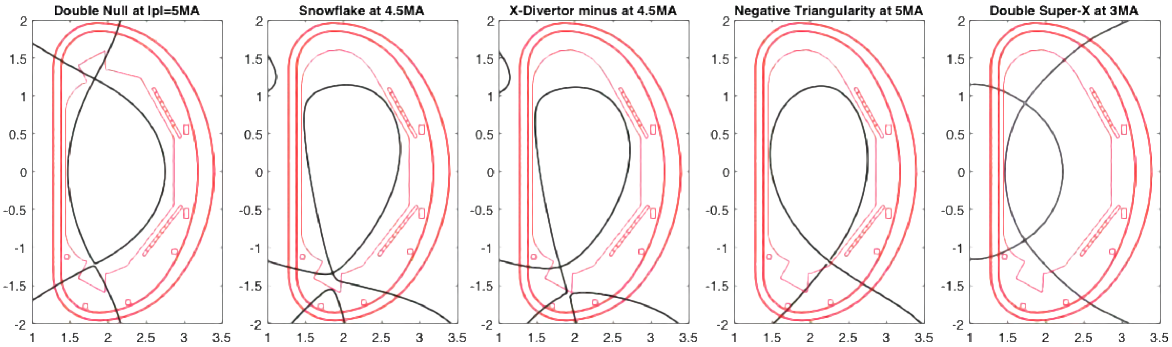

Figure 1.6: Some of the alternative magnetic configurations that can be studied by DTT. Image taken from [Mar+19].

1.3.2 Magnetic Systems

At the beginning of its operations DTT will operate in a Single-Null configuration with only a lower divertor. The magnet system is shown in a poloidal section in figure 1.7. It will have 18 Toroidal Field coils, 6 independent Central Solenoid coils as well as 6 Poloidal Field coils. There will also be 6 independent in-vessel coils of which four in the divertor region. Four of the PF coils will be made of Niobium-Titanium Cable-in-Conduit (CiC) superconductors with a maximum magnetic field between 4 and 5 T while the top and bottom one will have a maximum field of 8.5 T and will be made of Niobium-Tin CiC. These coils will have a top-down symmetry to allow the future installation of an upper divertor. Depending on the coil, their maximum current will be between 27.1 and 30 kA. The CS coils will each be made of two concentric sections, an High Field one that will reach up to 13.2 T and a Low Field one that will reach 9.4 T. The TF coils will reach a maximum field of 11.8 T and both these and the CS coils will be made of Nb_3Sn CiC.

Finally the in-vessel coils will be used both to determine with great precision the exhaust magnetic configuration and reduce the average heat flux on the divertor's target. For what concern the former, these coils will be able, for example, to generate double null regions in an hypothetical snowflake configuration with a large area with close to zero poloidal field and much more controllable flux flaring, thus reaching a condition much more ideal than what could be obtained with ex-vessel coils alone. For the latter, the coils will be used to implement feedback control strategies of the power flux by means of techniques like sweeping, where the position of the strike-points on the targets is made to move periodically [Amb+08], or wobbling, where the whole plasma is vertically displaced. While possible even without them, both of these techniques are implemented more easily and with much greater flexibility by the addition of these coils.

1.3.3 Heating and Current Drive

In order to obtain the exhaust heat fluxes required, DTT is expected to have external heating systems capable to provide up to 45 MW of power. These are of three types: Ion Cyclotron Resonance Heating, Electron Cyclotron Resonance Heating and Neutral Beam Injector.

The ICRH system will be made of a certain number of modules each composed of two antennas, both capable of generating 1.5 MW. Two possible design choices have been considered for the antennas, one based on those used on AUG, the other on those used on EAST. They will work in frequencies between 60 and 90 MHz at which between 55% and 65% of power is absorbed by electrons while the rest mostly by deuterium, with a small amount of heating to minority species. It will also be able to perform wall conditioning and, after the upgrade to full power, also generation of fast particles, density peaking, impurity accumulation and q-profile controls while current driving is not foreseen.

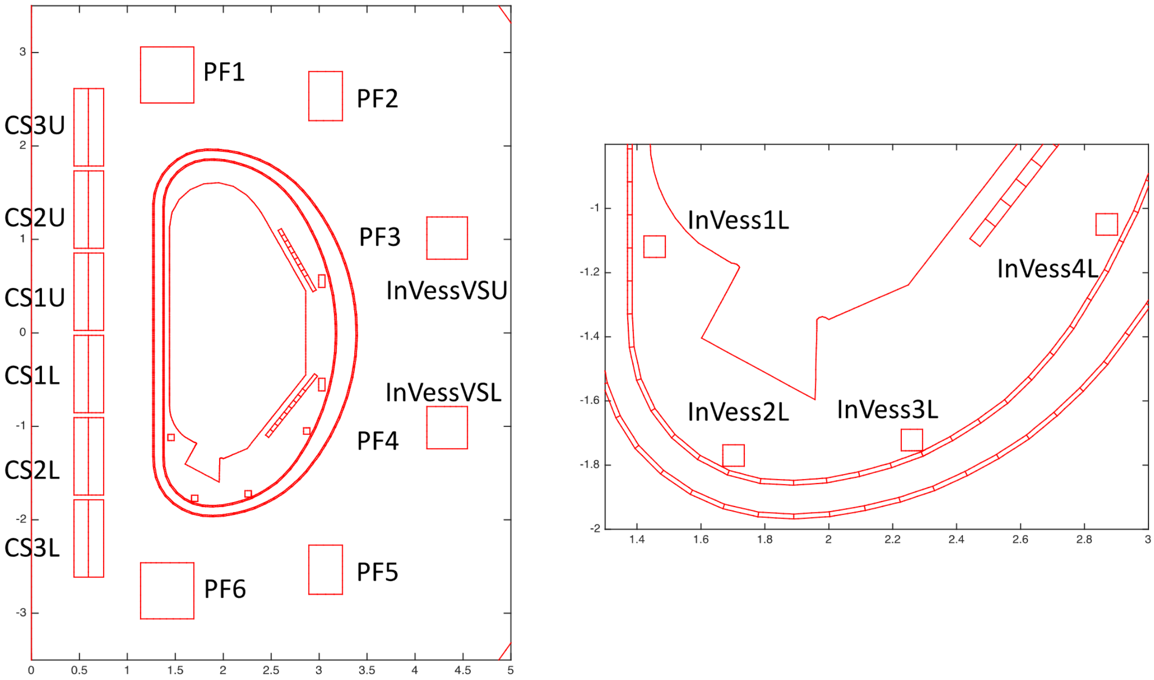

Figure 1.7: Poloidal section of the initial configuration of the DTT magnet system (left) and detail of the divertor region (right).

The ECRH system will be made of clusters, each consisting of 8 gyrotrons at 170 GHz and capable of injecting 8 MW of power. Every cluster will have 6 launching mirrors in an equatorial port and 2 in an upper port, all capable of independent poloidal and toroidal steering. The upper port injectors will be used for MHD activity and NTM stabilization even though the equatorial ones can be also used for such a task albeit with higher diffraction effects and wider current density profile. The whole system can be used for current drive with a maximum projected capability of $I_{\text{CD}}/P_0 \approx 15 - 20$ kA/MW and a current drive capability at the $q = \frac{3}{2}$ surface (at $\rho = 0.75$) of $I_{\text{CD}}/P_0 \approx 5$ kA/MW. The ECRH systems will also be used to assist at plasma start-up.

Finally the NBI system will consist of at least one negative-ion-based high energy injector, capable of delivering 7.5 MW of power. The acceleration potential will be 400 kV in two stages based on a simplified version of the MITICA design that will be used on ITER. This energy has been chosen to guarantee a sufficient plasma penetration and exploit existing work on high energy NBIs, in order to diminish costs and augment reliability. The injection angle will be of $42.4°$ at the first wall (the maximum possible due to the presence of the TF coils) to minimize shine-through and fast ion losses due to ripples in the toroidal field, at the cost of a wider power deposition distribution. The NBI will also be capable of current driving with a peak capacity of around $6 \cdot 10^5\,\text{A}\,\text{m}^{-2}$.

The total number of each of these systems has yet to be finalized. At the time of first commissioning (so called *day-0*) the machine will generate plasma at 3 T and 2 MA and will have only one ECRH cluster providing 8 MW. This will be increased to 25 MW in order to obtain H-mode in a 6 T plasma (*day-1* operations), with the installation of an additional ECRH cluster, 2 ICRH antennas and one NBI injector. The full-power operations will require a total of 45 MW of external heaters whose composition will be decided after the procurement of the first steps of the systems. The three option see the day-1 heaters plus 2 additional ECRH cluster and either a) an additional NBI, b) a further ECRH cluster or c) 4 additional ICRH antennas.

1.3.4 Diagnostics and Control

DTT will have several diagnostic systems for the main plasma in order to guarantee effective and safe operations but, in order to fulfill its scientific task, will be equipped with an extensive suite of sensors aimed at the plasma edge and at the divertor region.

A full description of the former would be beyond the scope of this work, but we will still provide a quick overview of some of them: two sets of 35 bi-axial pickup coils, one in- and one ex-vessel, will provide measurements of the current and plasma position. Other magnetic diagnostics include flux saddles and diamagnetic loops, Rogowski coils and resistive shunts. To assist equilibrium reconstruction other sensors will be used, including two interferometer polarimeters, a toroidal one operating at mid infrared and a poloidal one with grater spatial resolution operating at far infrared, and a reflectometer, capable of working both in X and O mode and using to frequency bands (W and D) due to the high densities and wide range of working magnetic fields (3 T and 6 T). In order to measure the kinetic profiles in the plasma core a Thomson scattering diagnostic will be used, mounting a Nd:YAG 1064 nm laser that will also measure the electron density, together with an ECE radiometer, charge exchange spectroscopy and a crystal spectrometer that will potentially be installed after the beginning of operations. These diagnostics will also be useful to detect non-Maxwellian components in the energy distribution that might play an important role in the plasma-wall interactions. Another important contribution to the characterization of power exhaust is given by fast ions that will be detected by $\gamma -$ ray detectors, on edge scintillator probes, Doppler shifted Balmer Alpha spectrometers and a collective Thomson scattering system. The presence of runaway electrons will be measured by hard X-ray and γ spectrometer detecting their Bremsstrahlung radiation, Cherenkov probes and finally cameras and spectrometers operating in visible light and NIR intercepting their forward emitted synchrotron radiation. Fission chambers, diamond detectors, activation foils and a neutron-γ camera will provide neutron measurements. The content and spatial distribution of impurities will be measured by bolometers, short wave length spectrometers and soft X-ray tomography that is also useful to monitor MHD activity in the plasma core. Finally several sensors will be used to study turbulence and fluctuating properties of the plasma, including Langmuir probes, gas puffing imaging and thermal helium beams.

Given the main scientific mission of DTT, a particular attention will be given to divertor diagnostics. The presence of neutral particles in the plasma edge will be detected by a TOF neutral particle analyzer and by a high resolution Dα spectrometer. In order to measure the electrons density and temperature a Thomson scattering system will be used, with an Nd:YAG 1064 nm laser entering from the bottom of the divertor. Emission spectroscopy will characterize the detachment state and position of the divertor plasma, together with the kinetics of the main species and impurities. Electrostatic sensors will provide measurements of both the value and fluctuations of poloidal profiles of electron current and density as well as divertor heat loads, the latter together with a large number of thermocouples. Finally, several visible and IR cameras will monitor plasma facing components.

The various diagnostics will be integrated in the real-time control of DTT through Proportional-Integral-Derivative (PID) and physics model based control schemes. Magnetic control will be particularly important in next generation machines both during the flat top and transient phases due to their strict requirements. In DTT the vertical stabilization of the plasma will be carried out using the in-vessel coils and a pair of passively stabilizing plates. The plasma shape control will be based on an eXtreme Shape Control (XSC) approach, already tested on JET and EAST and planned to be used on ITER, that will have to deal in particular with the high sensitivity to current fluctuation on alternative divertor magnetic geometries like the XD and snowflake that are to be studied in DTT. As already mentioned in subsection 1.3.2, the divertor coils will be tasked with thermal load management on the divertor targets by forcing a variation of the strike-points position through sweeping and wobbling. The ECRH system will be used to control Sawtooths and Neoclassical Tearing Modes, while active mitigation systems for Edge Localized Modes and Resistive Wall Modes (RWM) (external kink modes slowed down by the presence of a conducting wall around the plasma) are yet to be finalized. The same can be said of the disruption avoidance and mitigation systems. A Shattered Pellet Injector has been considered, with the added benefit of acting as a test bed for a similar solution being implemented in ITER.

1.4 Outline of this thesis

The aim of this work is to validate the RAPTOR code as faster-than-real-time simulation tool to be used in the future DTT experiment for feedback-loop control. In chapter 2 we will outline the problem to be solved and give an overview of the model used by RAPTOR, its implementation and simplifications. In chapter 3 we will use RAPTOR to simulate the plasma of DTT in two different scenarios: an early implementation of the experiment with limited magnetic field intensity, current and injected external heating power, called *scenario A*, and a full power scenario of the experiment representative of its final design capabilities, called *scenario E*. We will then confront the results derived by RAPTOR with those obtained with two other simulator codes, ASTRA for the scenario A and METIS for the scenario E. Finally, in chapter 4 we will test the ability of RAPTOR to simulate the behaviour of sawtooth instabilities in plasma by performing a simulated sweeping experiment.

Chapter 2

The plasma profile dynamics simulation problem and the RAPTOR code

2.1 The 1.5D model

Simulating the evolution of plasma in a tokamak reactor is a complex problem given the close interplay between the plasma itself and the magnetic fields confining it and the often empirical description of the physics behind its behaviour. It is also of the upmost importance for several reasons, both for finding the necessary inputs to achieve the desired plasma state before an experiment, to provide actual control in real time in transient and steady-state phases of the shot and finally to reconstruct the behaviour of the plasma after it.

As we will see, it's convenient to consider a series of nested surfaces determined by the poloidal field flux. Due to the symmetries of tokamak plasma, these will be determined by a series of concentric bi-dimensional contours over which several quantities of interest will either be constant or be reasonably approximated as such. These quantities will thus be determined by a series of one-dimensional radially dependant profiles. In this model the evolution of the plasma will be determined by both the evolution of these 2D contours, governed by MHD, and of the one-dimensional profiles, governed by transport phenomena, as well as by the coupling of these two aspects. As such the model is usually called the **1.5D tokamak plasma model** [Fel11]. The strategy to numerically simulate this evolution will be to find a way of reconstructing the contour geometry starting from the profiles (that, we will see, will take the form of the famous Grad-Shafranov equation), from this integrating the transport equations of the various profiles and thus computing their evolved state after one time step and finally to use this to find the new evolved geometry of the spatial contours.

Depending on the situation, we can distinguish between open-loop control systems, used to find the trajectory of the actuators needed to reach a determined flat-top state, and closed-loop, used to actually maintain this state for arbitrarily long time, using either feedback or adaptive

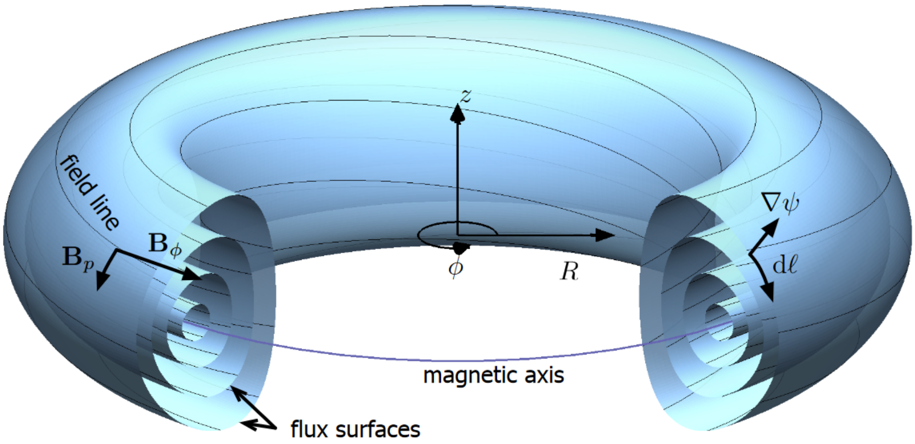

Figure 2.1: The toroidal coordinate system we will use to describe an axisymmetric plasma. Image taken from [Fel11]

control. In the latter case it's necessary to simulate the evolution of the plasma in a faster-than-real-time manner in order to have time to operate on the actuators and steer the system towards the desired condition. The kind of transport simulation codes able to be used in such applications are called *predictive*, meaning that they can solve the flux diffusion equation as well as finding the energy and particle profile evolution, opposed to the *interpretative* codes solving only the former and reading the latter from diagnostic data after a shot. Thus, from the need of solving a complex system of coupled differential equations relatively fast arises the necessity of lightweight codes making proper simplifications on the system to be studied while keeping all the relevant physics to give accurate predictions. This work is about one such simulators: **RAPTOR** (**Ra**pid **P**lasma **T**ransport simulat**OR**), a plasma transport code that will be implemented in the control system of DTT. In order to describe it, we will start in section 2.2 by deriving an equation able to determine the shape of flux surfaces, then in section 2.3 we will find the formulas describing the various transport and diffusion phenomena of interest. Finally, we will put these together in 2.4 by describing the actual RAPTOR physics model.

2.2 Flux functions and the Grad-Shafranov equation

In the following, we describe the equilibrium in a fusion device, using as reference [Wes11]. We will work on a cylindrical system of coordinates, with R as the distance from the central axis, z the position along the vertical direction and ϕ the azimuth angle that this case will be referred as the *toroidal* angle. The plane perpendicular to the toroidal direction will be called the *poloidal plane*. A schematic representation of the coordinate system is shown in figure 2.1. The first assumptions that we will make in the construction of our model is that each quantity we will deal with is independent from the toroidal angle ϕ so that our plasma will be *axisymmetric*. The second is that the plasma is in equilibrium and the magneto-hydrodynamic forces are balanced, leading to the condition

$$\mathbf{j} \times \mathbf{B} = \nabla p, \tag{2.1}$$

with the obvious consequence that pressure will be constant along magnetic field and current density lines.

The magnetic field, separated in its toroidal and poloidal components, will be written as

$$\mathbf{B} = \mathbf{B}_{\mathrm{p}} + B_\phi \, e_\phi$$

and will lay on nested magnetic surfaces around a circumference called the *magnetic axis*.

We then define the *poloidal flux function* $\psi(R, z)$ as the flux of poloidal magnetic field on a surface perpendicular to the central toroidal axis and going from the magnetic axis to one of the magnetic surfaces

$$\psi_{\mathrm{p}} = \int_0^{2\,\pi} d\phi \int_{R_{\mathrm{a}}}^{R_{\mathrm{b}}} R \, B_z(R, z = 0) \, dR$$

arbitrary to an additive constant.

We can then write the two components of the poloidal magnetic field in function of this flux as

$$B_z = \frac{1}{R}\frac{\partial \psi}{\partial R} \quad \text{and} \quad B_R = -\frac{1}{R}\frac{\partial \psi}{\partial z}, \tag{2.2}$$

in such a way that they will obey $\nabla \cdot \mathbf{B} = 0$. It's worth pointing out that $\nabla\psi \cdot B = 0$ and this means that ψ will be constant over the magnetic surfaces and that the geometries of the latter can thus be derived from the constant value contours of the former. Given that the pressure is also constant on these surfaces, we have that p can be written as a function of ψ.

Likewise, we can define a similar function $f(R, z)$ for the current density so that j_{p} can be written as

$$j_z = \frac{1}{R}\frac{\partial f}{\partial R} \quad \text{and} \quad j_R = -\frac{1}{R}\frac{\partial f}{\partial z}, \tag{2.3}$$

and that, similarly to ψ, f will be constant along current density lines. Now, given that p is constant over density lines, f will be a function of p and consequently of ψ. Thus, $f(\psi)$ and $p(\psi)$ are *flux functions* as they depend only on ψ. We now want to derive an equation that will allow us to reconstruct $\psi(R, z)$, and from that the magnetic geometry, knowing these functions.

We start by writing equation (2.1) as

$$\mathbf{j}_\mathrm{p} \times \mathbf{e}_\phi\, B_\phi + \mathbf{e}_\phi\, j_\phi \times \mathbf{B}_\mathrm{p} = \nabla p,$$

where $\mathbf{e}_\phi$ is the poloidal versor. Substituting in equations (2.2) and (2.3) we get

$$\frac{1}{R}(\nabla f \times \mathbf{e}_\phi) \times \mathbf{e}_\phi\, B_\phi + \mathbf{e}_\phi\, j_\phi \times \frac{1}{R}(\nabla \psi \times \mathbf{e}_\phi) = \nabla p.$$

With a bit of algebra and remembering that f and p are functions of ψ and that the derivatives along $\mathbf{e}_\phi$ must be null because of the axisymmetric condition, we get

$$-\frac{B_\phi}{R}\nabla f + \frac{j_\phi}{R}\nabla \psi = \nabla p \Rightarrow j_\phi = R\frac{dp}{d\psi} + B_\phi \frac{df}{d\psi}.$$

In order to eliminate j_ϕ and B_ϕ from this equation we use Ampere's Law $\mathbf{j} = \frac{1}{\mu_0}\nabla \times \mathbf{B}$, whose vertical and radial components

$$j_z = \frac{1}{R\mu_0}\frac{\partial(RB_\phi)}{\partial R} \quad \text{and} \quad j_R = -\frac{1}{\mu_0}\frac{\partial B_\phi}{\partial z}$$

compared with equ. (2.3) allows us to write

$$f = \frac{RB_\phi}{\mu_0},$$

while its poloidal component together with equ. (2.2) lends

$$\mu_0 j_\phi = \frac{dB_R}{dz} - \frac{dB_z}{dR} = -\frac{1}{R}\frac{\partial^2 \psi}{\partial z^2} - \frac{\partial}{\partial R}\left(\frac{1}{R}\frac{\partial \psi}{\partial R}\right).$$

Plugging all together we finally reach

$$\frac{\partial^2 \psi}{\partial z^2} + R\frac{\partial}{\partial R}\left(\frac{1}{R}\frac{\partial \psi}{\partial R}\right) = -\mu_0 R^2 p'(\psi) - \mu_0 f(\psi) f'(\psi), \tag{2.4}$$

known as the **Grad-Shafranov equation**. While this equation describes an equilibrium state, we can use it to study a non-equilibrium plasma as long as the time scales of the profile evolution of $f(\psi)$ and $p(\psi)$ and of the changes in the external actuators is slower than the typical MHD time scale. We can use for the latter the Alfén time,

$$\tau_A = a\frac{\sqrt{\mu_0\, \rho_m}}{B_0},$$

where a is the typical dimension of the device and ρ_m is the mass density of the plasma, that in case of fusion reactors is of the order of $\sim 1\,\mu$s.

2.3 Diffusion and transport phenomena

We now want to study how the profiles of the various quantities of interest evolve over time. Most of the following is described in detail in [HH76] and follows the notation used in [Fel11]. We start by finding the poloidal flux diffusion equation.

First, we define the *flux surface average* for a Q that is not a flux function as

$$\langle Q \rangle = \frac{\partial}{\partial V} \int_V Q \, dV$$

where V is the volume inside a given flux surface.

Then we can write the toroidal magnetic flux as

$$\Phi = \int \mathbf{B} \cdot d\mathbf{S}_\Phi = \frac{1}{2\pi} \int_V \frac{\mu_0 f}{R^2} dV.$$

We finally define a new flux coordinate, the effective minor radius coordinate ρ, as

$$\rho = \rho_{\text{tor}} = \sqrt{\frac{\Phi}{\pi B_0}}.$$

This quantity is a measure of the characteristic size of the cross section of the poloidal surface and we will use it as a label for the flux surfaces instead of ψ. Note that on the magnetic axis $\rho = 0$ and we will call ρ at the Last Closed Flux Surface ρ_e. When discussing the results of RAPTOR we will work with the renormalized version of this value, simply defined as $\hat{\rho} = \rho/\rho_e$.

We can then consider the component of Ohm's law parallel to the magnetic field, averaged over a flux surface

$$j_{||} = \sigma_{||} E_{||} + j_{\text{bs}} + j_{\text{cd}}$$

where $\sigma_{||}$ is the neoclassical conductivity, j_{bs} is the bootstrap current, i.e. the current generated by particle trapped in banana-like orbits due to the varying intensity of the magnetic field, and j_{cd} is the current generated by external driver systems like neutral beam injectors and cyclotron resonant heaters.

By writing the parallel current density and electric field as functions of ψ we can get the **poloidal current diffusion equation**

$$\sigma_{||} \left(\frac{\partial \psi}{\partial t} + \frac{\rho \dot{B}_0}{2 \, B_0} \frac{\partial \psi}{\partial \rho} \right) = \frac{R_0 J^2}{\mu_0 \rho} \frac{\partial}{\partial \rho} \left(\frac{G_2}{J} \frac{\partial \psi}{\partial \rho} \right) - \frac{V'}{2\pi\rho} (j_{\text{bs}} + j_{\text{cd}}) \tag{2.5}$$

where

$$J = \frac{\mu_o \, f}{R_0 \, B_0}, \quad G_2 = \frac{V'}{4\pi^2} \left\langle \frac{(\nabla \rho)^2}{R^2} \right\rangle, \quad V' = \frac{\partial V}{\partial \rho}.$$

Given that the magnetic flux is zero on the magnetic axis the boundaries condition at $\rho = 0$ is

$$\left.\frac{\partial \psi}{\partial \rho}\right|_{\rho=0} = 0.$$

Meanwhile the boundary condition at $\rho = \rho_e$ can be expressed in two ways depending if we are dealing with an actual experiment where we only know the voltage in the tokamak coil system or we have the value of the total plasma current. In the first case it will take the form

$$L_{\text{ext}}\left[\frac{G_2}{\mu_0}\frac{\partial \psi(\rho,t)}{\partial \rho}\right]_{\rho=\rho_e} + \psi(\rho,t)|_{\rho=\rho_e} = \int_{t_0}^{t} V_{OH}\, dt$$

where L_{ext} is the external inductance of the plasma and V_{OH} is the voltage in the coil system.

In the second case we instead have

$$\left[\frac{G_2}{\mu_0}\frac{\partial \psi(\rho,t)}{\partial \rho}\right]_{\rho=\rho_e} = I_p(t)$$

where $I_p(t)$ is the externally induced plasma current.

We now write the transport equations for a generic species α in the plasma. Its continuity equation will be

$$\frac{\partial n_\alpha}{\partial t} + \nabla \cdot (n_\alpha \, \mathbf{u}_\alpha) = s_\alpha,$$

where n_α is the local number density, $\mathbf{u}_\alpha$ is the local velocity and s_α is the localized particle source. By integrating this equation over the volume contained in a flux surface and after a series of mathematical passages we obtain the **equation for particle transport** inside one such surface:

$$\frac{1}{V'}\left(\frac{\partial}{\partial t} + \frac{\dot{B}_0}{2B_0}\frac{\partial}{\partial \rho}\rho\right)(\langle n_\alpha\rangle V') + \frac{1}{V'}\frac{\partial}{\partial \rho}\big[V'\langle n_\alpha(\mathbf{u}_\alpha - \mathbf{u}_\Phi)\cdot\nabla\rho\rangle\big] = \langle s_\alpha\rangle. \tag{2.6}$$

Similarly, one can obtain the **equation for energy transport** for a specific species:

$$\frac{3}{2}\Big(V'\Big)^{\frac{5}{3}}\left(\frac{\partial}{\partial t} + \frac{\dot{B}_0}{2B_0}\frac{\partial}{\partial \rho}\rho\right)\left[\Big(V'\Big)^{-\frac{5}{3}} n_\alpha T_\alpha\right] + \frac{1}{V'}\frac{\partial}{\partial \rho}\left(q_\alpha + \frac{5}{2}T_\alpha\Gamma_\alpha\right) = P_\alpha, \tag{2.7}$$

where P_α is the net power that will be different depending on the species, while Γ_α and q_α are the convective and diffusive heat fluxes that can be expressed as

$$\Gamma_\alpha = -V'G_1 n_\alpha\left[\sum_{\beta\,\in\,\text{species}}\left(D^\alpha_{n_\beta}\frac{1}{n_\beta}\frac{\partial n_\beta}{\partial \rho} + D^\alpha_{T_\beta}\frac{1}{T_\beta}\frac{\partial T_\beta}{\partial \rho}\right) + D_E\frac{E_\|}{B_p}\right]$$

$$q_\alpha = -V' G_1 T_\alpha n_\alpha \left[\sum_{\beta \,\in\, \text{species}} \left(\chi^\alpha_{n_\beta} \frac{1}{n_\beta} \frac{\partial n_\beta}{\partial \rho} + \chi^\alpha_{T_\beta} \frac{1}{T_\beta} \frac{\partial T_\beta}{\partial \rho} \right) + \chi_E \frac{E_\parallel}{B_p} \right],$$

where T_α is the temperature of the species, $D^\alpha_{n_\beta}$ and $\chi^\alpha_{n_\beta}$ are the particle and heat transport coefficients for fluxes caused by a gradients in the density of species β, while $D^\alpha_{T_\beta}$ and $\chi^\alpha_{T_\beta}$ are the same for temperature gradients. These are dependent on ρ and the various profiles and finding their value is a non trivial problem. Finally G_1 is a geometrical quantity defined as

$$G_1 \equiv \left\langle (\nabla \rho)^2 \right\rangle.$$

A Neumann boundary condition is used for both equations (2.6) and (2.7) at $\rho = 0$ to impose a zero net flux

$$\left. \frac{\partial n_\alpha}{\partial \rho} \right|_{\rho=0} = 0, \qquad \left. \frac{\partial T_\alpha}{\partial \rho} \right|_{\rho=0} = 0,$$

while for $\rho = \rho_e$ a Dirichlet boundary condition is usually utilized with externally imposed density and temperature at plasma edge.

It is at this point useful, for the sake of solving the 1.5D tokamak problem, to rewrite equation (2.4) in terms of quantities we can compute by solving the transport equations. We obtain

$$\frac{\partial^2 \psi}{\partial z^2} + R \frac{\partial}{\partial R} \left(\frac{1}{R} \frac{\partial \psi}{\partial R} \right) = 2\pi \mu_0 R_0 \left[\frac{J}{\langle B^2 / B_0^2 \rangle} \left(j_\parallel \frac{R_0 J}{B_0 \rho \iota} \frac{\partial p}{\partial \rho} \right) - \frac{R^2}{B_0 R_0 \rho \iota} \frac{\partial p}{\partial \rho} \right], \tag{2.8}$$

where ι is the rotational transform of the plasma and is the reciprocal of the safety factor q. It can be defined as

$$\iota = \frac{1}{q} = \frac{\partial \psi}{\partial \phi} = \frac{1}{2\pi B_0 \rho} \frac{\partial \psi}{\partial \rho}.$$

2.4 The RAPTOR code physics model

We will now go over the basic assumptions of the RAPTOR code and a description of its implementation.

Solved equations and geometry RAPTOR uses a purely 1D transport model and can solve the flux transport equation for $\psi(\rho, t)$ equ. (2.5) and the transport equations for $T_\alpha(\rho, t)$ equ. (2.7) and $n_\alpha(\rho, t)$ equ. (2.6) for both ions and electrons. In previous implementations of the code, the profiles of n_i, n_e and T_i could only be externally fixed while in the current iteration they can also be solved. [Fel+18b]

The plasma geometry will be externally prescribed by passing as time-varying inputs all the variables dependent on the magnetic geometry, in particular J, V', G_1 and G_2. Note that this doesn't mean that the whole Grad-Shafranov equilibrium is externally fixed, only the shape of the poloidal flux surfaces. An alternative it's to couple RAPTOR with an external equilibrium code to calculate the solutions of the G-S equation.

Sources and sinks Both external heating and current drives can be simulated in two ways: either by a complete external prescription as a ρ dependant profile, or approximated by using a gaussian profile. In the latter case the heating power for the ith actuator for the species α is given as

$$P_{\alpha,\,i}(\rho,t) = A\,P_i(t)e^{-\frac{4(\rho-\rho_{\text{dep},\,i})^2}{\omega^2_{\text{dep},\,i}}} \quad \text{with}\ \frac{1}{A} = \int_0^{\rho_e} e^{-\frac{4(\rho-\rho_{\text{dep},\,i})^2}{\omega^2_{\text{dep},\,i}}}\ V'\,d\rho,$$

where $\rho_{\text{dep},\,i}$ is the depth of maximum deposition and $\omega_{\text{dep},\,i}$ is the deposition width, while the current drive will be

$$j_{cd\,\alpha,\,i}(\rho,t) = c_{cd}e^{\frac{\rho^2}{0.5^2}}\frac{T_e}{n_e}P_i(t)e^{-\frac{4(\rho-\rho_{\text{dep},\,i})^2}{\omega^2_{\text{dep},\,i}}}$$

where c_{cd} is a machine dependant constant. This equation is derived from heuristic considerations on the dependence of the efficiency of external current drives on temperature, density and trapped particle fraction.

Transport models Several transport models have been implemented in RAPTOR in order to calculate the values of the coefficients used in the profile evolution equations, namely χ_s, D_s and V_s. The most simple and first to be implemented makes use of an empirical expression to find the thermal diffusion coefficient:

$$\chi_s = \chi_{\text{neo}} + c_{\text{ano}}\,\rho\,q\left[\frac{a_{ic}}{1+e^{\omega_{ic}(d_{ic}-s)}} + 1 - a_{ic}\right] + \chi_{\text{central}}e^{-\frac{\rho^2}{\delta_0^2}},$$

where the first term is a constant representing neo-classical diffusion, the last term derives from experimental observations on confinement decrease at the center of plasma and the middle term is a shear dependent term representing anomalous diffusion and improved confinement scenarios, with a_{ic}, ω_{ic} and d_{ic} as user defined parameters.

Another possible model, and the one used in this work, is a mixed Bohm-gyroBohm as described in [Erb+98]. The coefficient is given by two terms:

$$\chi_s^{\text{M}} = \chi_s^{\text{B}} + \chi_s^{\text{GB}}$$

with the first term being

$$\chi_s^{\text{B}} = \alpha_s^{\text{B}}\frac{c\,T_s}{e\,B}\frac{a\,\nabla p_s}{p_s}q^2 \propto \frac{c|\nabla p_s|}{e\,n_s\,B}a\,q^2.$$

This is an empirical term that is heavily dependent on the machine characteristics and for this reason is the second gyro-Bohm-like term is added:

$$\chi_s^{\mathrm{GB}} = \alpha_s^{\mathrm{GB}} \frac{c\,T_s}{e\,B} \rho \frac{a\,\nabla T_s}{T_s} \propto \sqrt{T_s} \frac{|\nabla T_s|}{B^2}.$$

The α's are various externally fixed parameters, whose value found in literature as $\alpha_e^{\mathrm{B}} = \frac{1}{2}\alpha_i^{\mathrm{B}} = 2.5 \cdot 10^{-4}$ and $\alpha_e^{\mathrm{GB}} = \alpha_i^{\mathrm{GB}} = 3.5 \cdot 10^{-2}$. The values that give the best results can however be considerably different.

It's also worth pointing out that in alternative RAPTOR can derive the heat and particle transport coefficients using QLKNN-4Dkin, a neural network regression of the QuaLiKiz quasi-linear gyrokinetic transport model, based on a training set of one hundred thousands profiles and allowing to obtain analytical derivatives of the coefficients with respect to the profiles allowing fully implicit solutions of the transport equations [Fel+18a].

Neoclassical conductivity The neoclassical conductivity is given by the Spitzer conductivity multiplied by a radially dependent neoclassical correction term

$$\sigma_{\|}(\rho,t) = c_{\mathrm{neo}}(\rho) \frac{1.9012 \cdot 10^4\, T_e[\mathrm{eV}]^{\frac{3}{2}}}{Z\,N(Z)\,\log \Lambda_e},$$

where instead of a $Z(\rho)$ it's taken an effective atomic number Z_{eff} constant over all the plasma, $N(Z)$ is a parameter with a weak dependence on Z and $c_{\mathrm{neo}}(\rho)$ depend on the geometry of the plasma and is evaluated only once for each equilibrium, thus ignoring small changes caused by variations in collisionality.

Bootstrap current Neoclassical effects in a tokamak are responsible for peculiar orbits of some of the particles in the plasma that, instead of gyrating on the poloidal plane, move poloidally back and forth in a so called banana orbit, due to the shape of its projection on the poloidal plane. If a density gradient is present, this results in a net current called diffusion driven current or bootstrap current that can be an important component of the toroidal current.

The value of the bootstrap current in RAPTOR is

$$j_{\mathrm{bs}} = -2\pi J(\psi) R_0 p(\psi) \left[\mathcal{L}_{31} \frac{\partial \log(n_e)}{\partial \psi} + \frac{p_e}{p} (\mathcal{L}_{31} + \mathcal{L}_{32}) \frac{\partial \log(T_e)}{\partial \psi} + \left(1 - \frac{p_e}{p}\right) (\mathcal{L}_{31} + \alpha \mathcal{L}_{34}) \frac{\partial \log(T_i)}{\partial \psi} \right]$$

with the additional assumption that in the cases where the temperature profile of ions and electrons are very different j_{bs} is small so we can simplify $\frac{\partial \log(T_e)}{\partial \psi} = \frac{\partial \log(T_i)}{\partial \psi}$ in the equation. The coefficients α, $\mathcal{L}_{31}$, $\mathcal{L}_{32}$ and $\mathcal{L}_{34}$ are radially dependant, determined by the geometry of the system and can be externally prescribed.

Instabilities RAPTOR is capable of modelling the effect of sawtooths crashes. This is done in two phases, first by introducing a condition for the onset of the crashes and then by modifying the affected profiles as a consequence. The first step is makes use of the Porcelli crash criterion [PBR96]. This is based on the definition of an energy functional for the $n = m = 1$ kink instability in the plasma

$$\delta W = \delta W_{\text{mhd}} + \delta W_{\text{KO}} + \delta W_{\text{fast}}$$

constituted by a magneto-hydrodynamic term and a fast particles and a Kruskal–Oberman stabilizing terms linked to collisionless trapped thermal ions. The crash can occur when this functional is close to zero near the $q = 1$ surface (plus other conditions) and this leads to a series of possible thresholds on the renormalized functional and the $q = 1$ magnetic shear s_1:

$$-\delta\hat{W}_{\text{mhd}} + \delta\hat{W}_{\text{KO}} > c_{\text{h}}\omega_{\text{Dh}}\tau_{\text{A}}$$

$$-\delta\hat{W} > 0.5\,\omega_{*\text{i}}\tau_{\text{A}}$$

$$-c_\rho\hat{\rho} < -\delta\hat{W} < 0.5\,\omega_{*\text{i}}\tau_{\text{A}} \quad \text{and} \quad s_1 > s_{\text{crit}}$$

where τ_{A} is the Alfvén time, $\omega_{*\text{i}}$ is the ion drift wave frequency and s_{crit} is given by

$$s_{\text{crit}} = 1.5\,c_*^{-\frac{7}{6}}\left(\frac{T_e/T_i}{1+T_e/T_i}\right)^{\frac{7}{12}}\sqrt{S^{\frac{1}{3}}}\left(\frac{\beta_{i1}R^2}{\overline{r}_1^2}\right)^{\frac{7}{12}}\frac{\overline{r}_1}{r_n}\left(\frac{\overline{r}_1}{r_p}\right)^{\frac{1}{6}}$$

where β_{i1} is the ion poloidal beta, r_p is the pressure scale length, r_n is the density scale length and $\overline{r}_1$ is the average $q = 1$ surface radius. The fixed parameters c_*, c_{h} and c_ρ are of the order of unit.

The second step is the profile modification using a Kadomtsev full reconnection model [Kad75], where lines of equal helicity at two different radii connect and a new single circular surface with the same helicity and radius between the initial two is formed. This new radius r_K is chosen so that the area enclosed in the new surface is equal to the area of the ring section between the initial one, i.e.

$$r_K^2 = r_2^2 - r_1^2.$$

This surface conserves the sum of total particles and energy from the two initial surfaces and allows to recompute the new temperature profile.

RAPTOR is also capable of modelling Neoclassical Tearing Modes. In order to do that it calculates self-consistently the width and frequency evolution of the tearing mode using a Rutherford model. Once the size and position of the magnetic island has been determined, a gaussian correction to the transport coefficients in that area is added to qualitatively simulate the effect of enhanced transport inside it.

Spatial discretization RAPTOR uses a spatial parametrization bases on finite elements with non-periodic cubic B-splines as basis functions defined by a set of non-equidistant knots, so that there is continuity up to the second derivative and with zero derivative at $\rho = 0$ to identically satisfy the Neumann boundary conditions we defined in the previous section. The generic transport equation to be solved for the variable $y(\hat{\rho},t)$ is

$$m_y \frac{\partial y}{\partial t} = \frac{\partial}{\partial \hat{\rho}}(a_y y) + \frac{\partial}{\partial \hat{\rho}} d_y \frac{\partial y}{\partial \hat{\rho}} + h_y T_e + s_y,$$

where the variable is rewritten as a sum of splines $y(\hat{\rho},t) = \sum_i^{n_{sp}} \Lambda_\alpha(\rho)\hat{y}_\alpha$. By multiplying for a set of trial functions Λ_β and integrating by part over $\hat{\rho}$ to remove the second-order derivative terms the PDEs are recasted as a set of nonlinear ordinary differential equations:

$$\mathbf{M}_y \hat{\mathbf{y}}' = (-\mathbf{A}_y - \mathbf{D}_y + \mathbf{H}_y)\hat{\mathbf{y}} + \mathbf{l} + \mathbf{s}.$$

The various variables to be solved are combined in a state vector and the differential equations written as

$$0 = \tilde{f}(\dot{x}(t),x(t),z(t))$$

with $z(t)$ containing all external time-dependent variables.

Time discretization The time discretization happens on a time grid with possible varying time step with a backward Euler method as

$$\dot{x}(t_k) = \frac{x_{k+1} - x_k}{\Delta t} \quad \text{and} \quad x(t_k) = x_{k+1}$$

where a fully implicit method has been chosen to allow relatively long time steps without stability problems. This nonlinear equation is then solved through Newton-Raphson iterations.

Chapter 3

Simulation data sets

3.1 Simulation of scenario A and comparison with the results obtained with ASTRA

3.1.1 Scenario A description and inputs

Scenario A will be the first of the initial phase of DTT operations, with just one ECRH cluster capable of injecting up to 8 MW of external power. It will test both Single-Null, X-divertor and NT configurations, but the simulation considered in this work will be of the first in H-mode. For a SN configuration scenario A generally entails a plasma current $I_p = 2\,\text{MA}$, a $B_0 = 3\,\text{T}$, $q_{95} = 3.87$, $k_{95} = 1.64$, $\delta_{95} = 0.31$ and $\beta_p = 0.3$ [CGM+24].

RAPTOR was set up in order to simulate the scenario A by solving the equations for T_e, T_i and ψ. Our specific simulation lasts up to the 14th second of a discharge, with a plasma ramp up (RU) and the initial portion of the flat top, the latter starting from $t = 5$ s together with the formation of the divertor X-point. The plasma current has been made to rise with a ramp up to a value of 2 MA at the beginning of flat top, then it remains constant. The density profiles of ions and electrons are equal and the values computed by ASTRA are taken as inputs. Both the input current and densities at plasma center are shown in fig. 3.1 while two radial density profiles used as input are shown in figure 3.2, one during the RU before H-mode activation and the other during FT in H-mode. The on-axis toroidal magnetic field has been imposed as $B_0 = 3$ T for the whole discharge. A Bohm-gyroBohm model has been used for the heat transport coefficients. The empirical parameters have been tuned to obtain results as close as possible to those of ASTRA and taken as $\alpha_{Be} = 2.5 \cdot 10^{-6}$, $\alpha_{Bi} = 2.5 \cdot 10^{-7}$, $\alpha_{gBe} = 5 \cdot 10^{-3}$ and $\alpha_{gBi} = 5 \cdot 10^{-4}$. The Porcelli criterion has been chosen to simulate sawtooth crashes with a full reconnection model for the temperature and q profiles, with a critical shear for reconnection equal to 0.2. As already mentioned, only the ECRH system is active. It has a gaussian deposition profile with maximum at $\hat{\rho}_{\text{dep}} = 0.28$, width $\omega_{\text{dep}} = 0.1$ and with a total injected power of 1.8

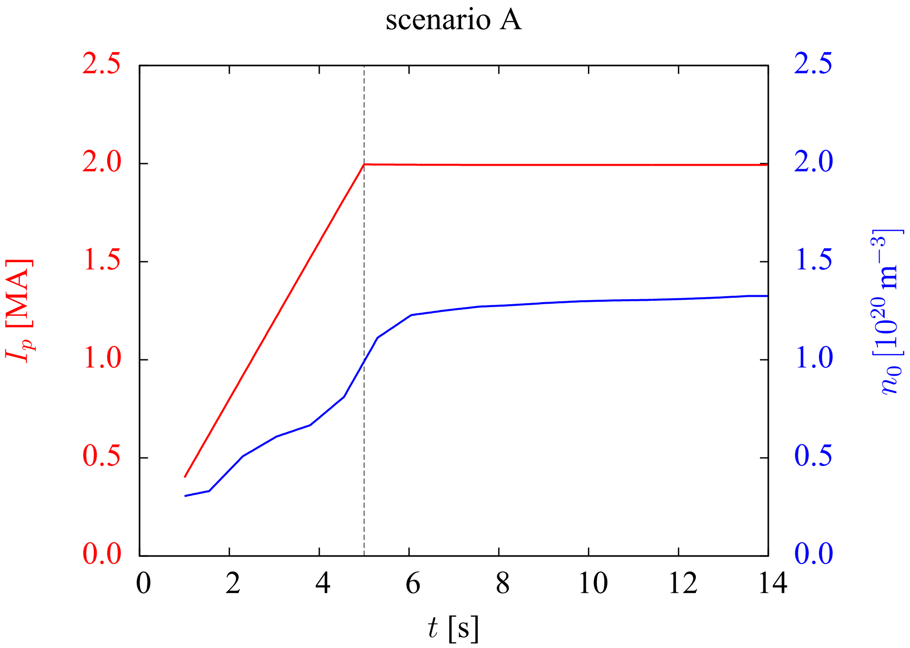

Figure 3.1: Plasma current and particle density at $\hat{\rho} = 0$ (equal for ions and electrons) used by ASTRA. These values (along with the full radially dependant density profile) have been used as inputs for RAPTOR. The beginning of the flat top is highlighted.

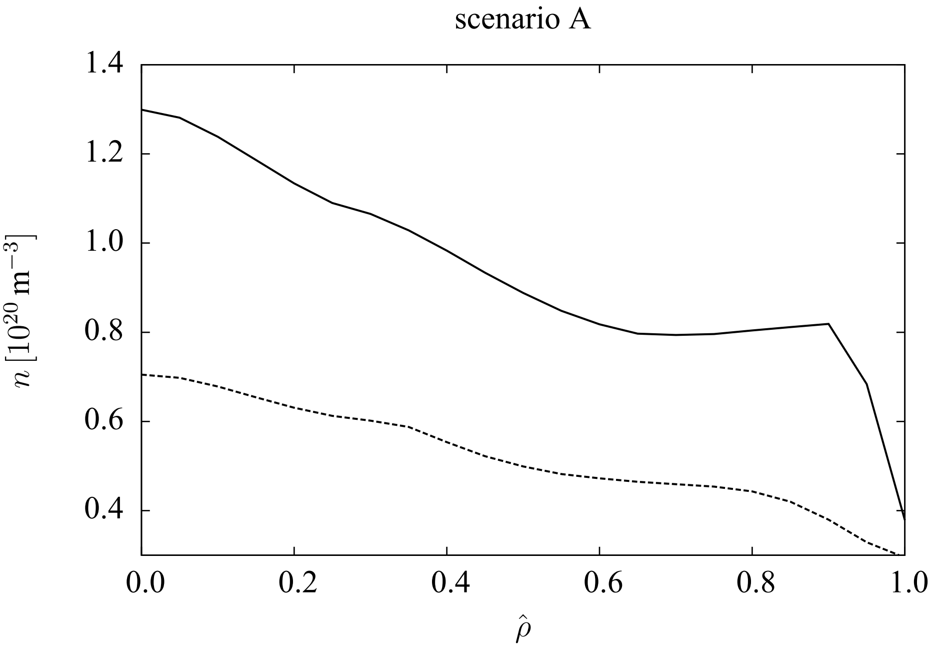

Figure 3.2: Ions and electrons numerical density profiles in function of $\hat{\rho}$ at $t = 4$ s (dashed line) and at $t = 10$ s (continuous line) used by ASTRA and given as input to RAPTOR. Both these profiles are the results of a linear interpolation between two pairs of instants in the ASTRA time grid, between $t = 3.80$ s and $t = 4.55$ s for the dashed line and between $t = 9.80$ s and $t = 10.55$ s for the continuous line.

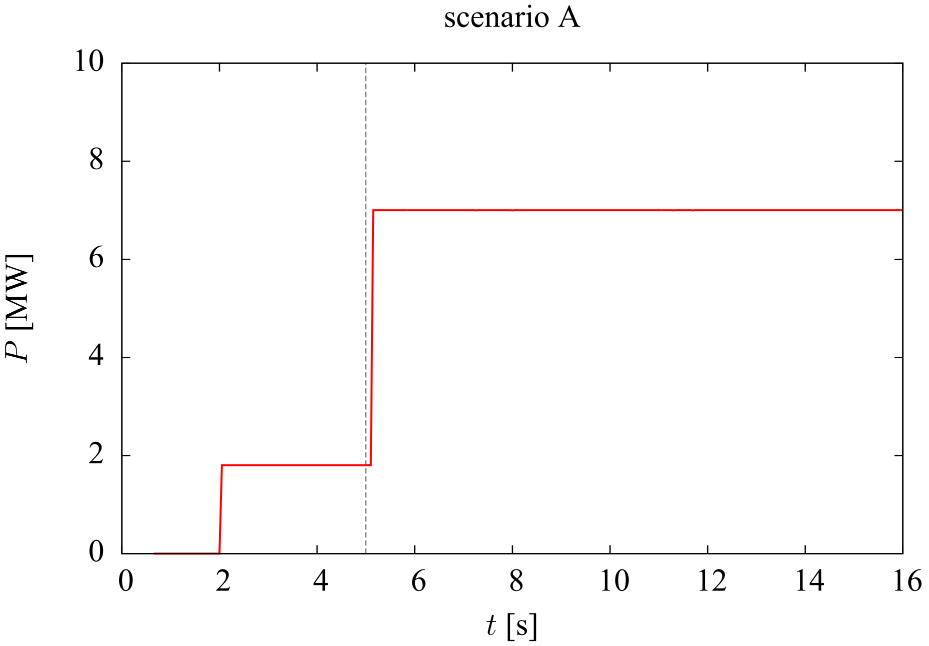

Figure 3.3: Total power injected by the ECRH system in function of time for the scenario A simulation. The beginning of the flat top is highlighted.

MW for $2 < t < 5$ s and 7 MW for $5 < t < 15$ s. The total power injected as function of time is shown in figure 3.3. The H-mode module has been activated at $t = 4.6$ s with a transport barrier at $\hat{\rho}_{\text{ped}} = 0.9$ and temperatures at the top of the pedestal taken as input from the ASTRA simulation. Before the start of the H-mode the edge temperature from ASTRA have been used as time-varying boundary conditions. The values of effective charge of the ions and the profile of thermal losses due to radiation have also been imported from ASTRA, as well as all the initial conditions for the plasma state. The standard bremsstrahlung module of RAPTOR has been used. The magnetic equilibria have been provided as a set of EQDSK files generated with the CREATE-NL+ free boundary condition plasma equilibrium solver [AAM15] and processed with the CHEASE code [LBS96]. The radial mesh is made of equidistant point with a spacing equal to $\hat{\rho} = 0.05$ for a total of $n_{sp} = 21$ points. The time grid is made of constant time steps of 0.05 s. All the time varying and/or radially dependent inputs have been linearly interpolated over these grids.

3.1.2 The ASTRA modelling tool

ASTRA (**A**utomated **S**ystem for **TR**ansport **A**nalysis) is a physics oriented, highly customizable plasma transport modelling suite [PY02]. Rather than being a single simulator, it provides an environment to build specific customized codes. It has been created to be highly flexible and allows the user to chose between a great number of possible modules to produce a simulation tailored to each specific problem, with capability both of background running or active control at runtime. Like RAPTOR, it solves the transport equations in a axisymmetric plasma within a 1.5D model, with different possible choices of initial and boundary conditions. ASTRA can additionally solve truncated forms of the transport equations to model the behaviour of other hydrogen isotopes, helium ashes, impurities and non-Maxwellian populations of the main plasma. It can also solve a kinetic equation for a neutral distribution function to model the effect of gas puff neutrals. The ASTRA library contains roughly one hundred different possible values for transport coefficients, as well as modules for simulating HCD systems, Tearing Modes and sawtooth crashes using the Kadomtsev theory.

3.1.3 Results

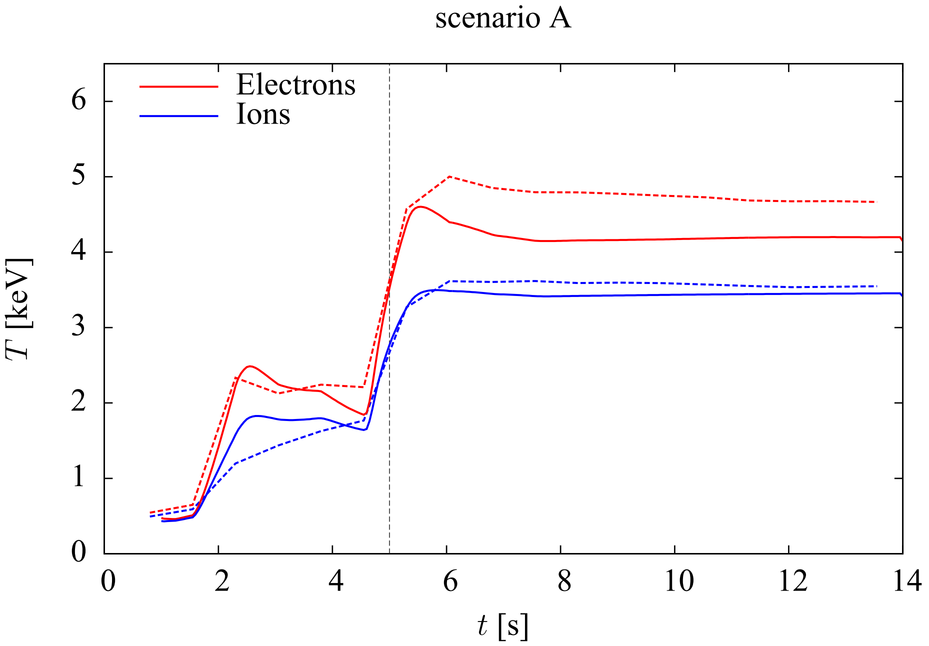

Figure 3.4: Ions and electrons temperature at $\hat{\rho} = 0$ for the simulations of scenario A done with RAPTOR (continuous line) and ASTRA (dashed line). The beginning of the flat top is highlighted.

The results show a good accordance between RAPTOR and ASTRA. In figure 3.4 we can see the temperature dynamic at the center of the plasma for all the discharge. Note that during the plasma ramp up its value doesn't deviate significantly from ASTRA, with the major difference in the ion temperature at $t = 3$ s. One possible explanation for the difference in that particular moment is that there is a relatively high discrepancy between the time evolution of the ion and electron temperature in ASTRA that is more difficult for RAPTOR to follow because of the stricter coupling in its heat transport equations for the different species. During flat top we see

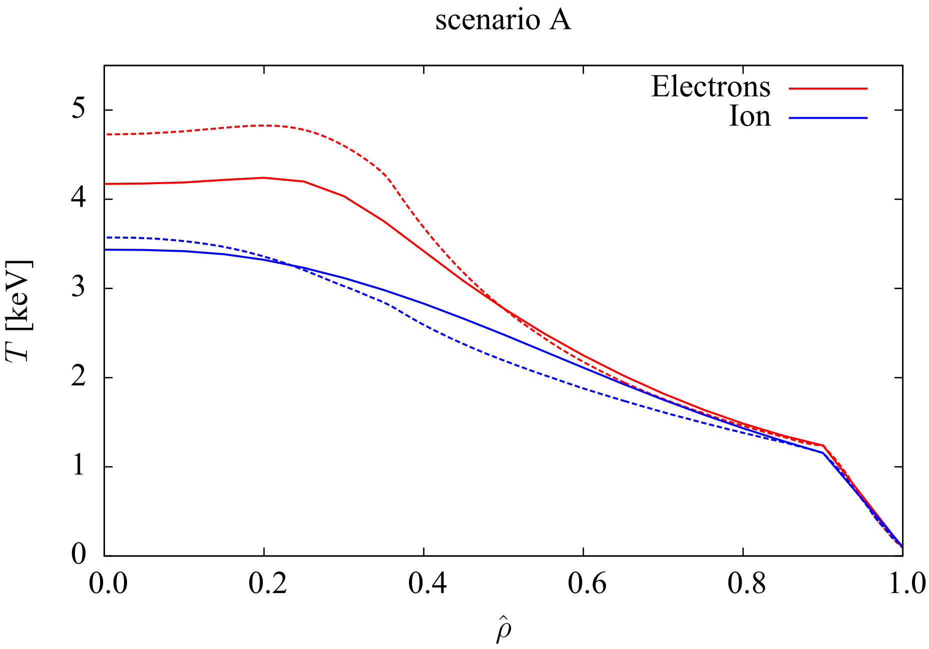

Figure 3.5: Ions and electrons temperature profiles in function of $\hat{\rho}$ at $t = 10$ s for the simulations of scenario A done with RAPTOR (continuous line) and ASTRA (dashed line).

that instead the ion temperature is closer between the two simulations while the electron one has a difference of the order of 0.5 keV. To better understand it we consider figure 3.5, where we can see the comparison of a typical temperature profile of RAPTOR and ASTRA during FT. Note that the electron temperature profile follows the same shape with a less accentuated peaking near the core, causing the underestimation of core temperature. Meanwhile the ion profile has a well defined inflection point in RAPTOR but the absolute difference is lower on average. To numerically quantify the difference we use a standard deviation figure of merit defined as

$$\sigma_T^s(t) = \sqrt{\frac{\sum_{i=1}^{n_{sp}} \left(T_{s,i}^{\mathrm{R}}(t) - T_{s,i}^{\mathrm{A}}(t)\right)^2}{\sum_{i=1}^{n_{sp}} \left(T_{s,i}^{\mathrm{A}}(t)\right)^2}}, \tag{3.1}$$

where $T_{s,i}^{\mathrm{R}}(t)$ and $T_{s,i}^{\mathrm{A}}(t)$ are the temperatures of the s specie (ions or electrons) at the instant t evaluated on the ith point of the spatial mesh in RAPTOR and ASTRA respectively. The results are shown in figure 3.6. While the discrepancy is relatively high during flat top, reaching 20% for the electrons and 40% for the ions, it stabilises between 10% and 15% for the former and below 10% for the latter during flat top. The discrepancies can have a number of explanation, including differences in the heat transport model or in the ohmic power released in the plasma between RAPTOR and ASTRA.

The evolution of the safety factor q in the two simulations is shown in 3.7, where in particular we can see its value at the center and edge of the plasma. While the value of q_{95} is in very good

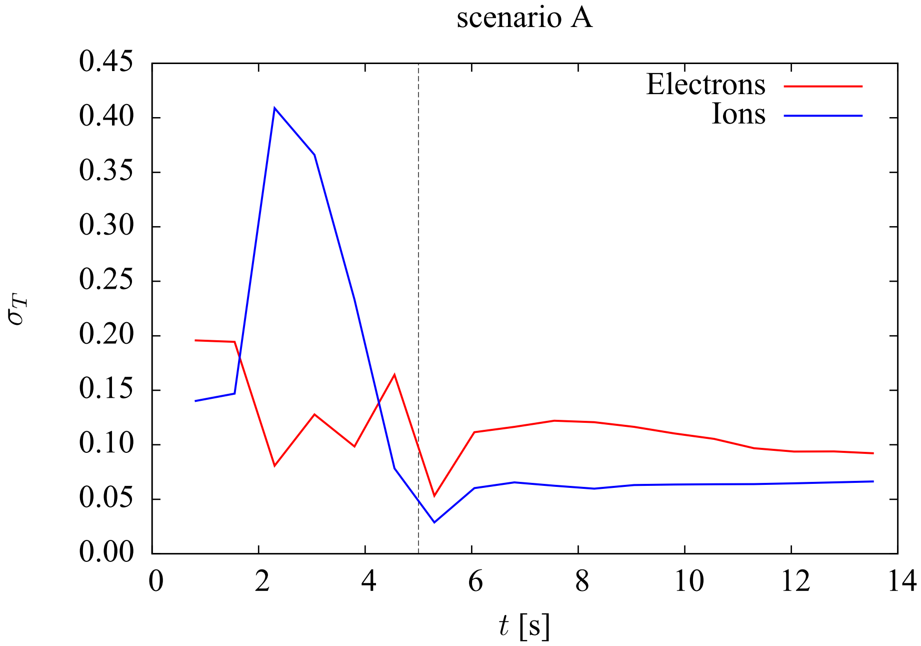

Figure 3.6: Normalized standard deviation between the temperatures computed by RAPTOR and ASTRA in the simulation of the scenario A. The beginning of the flat top is highlighted.

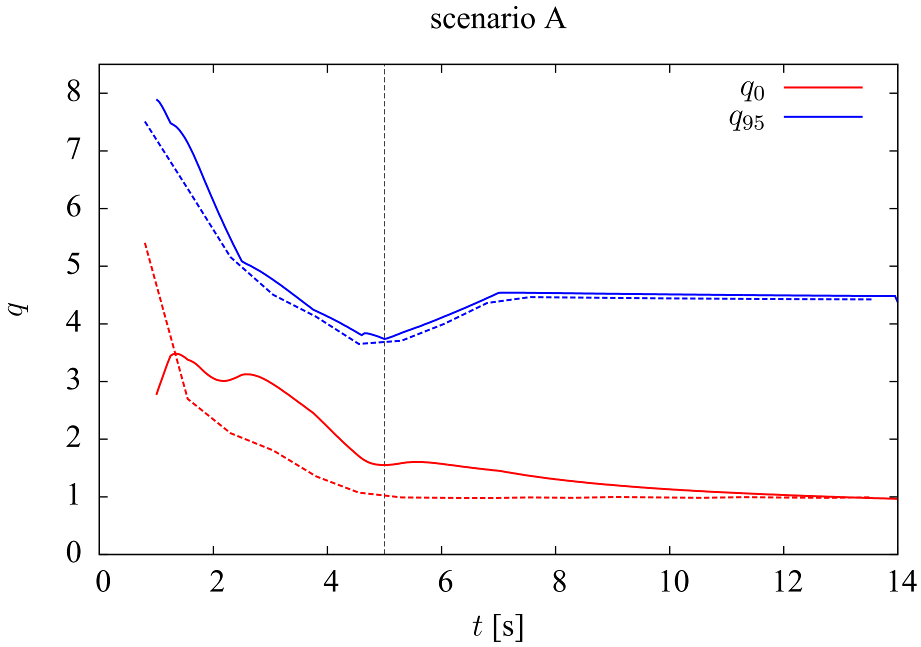

Figure 3.7: Values of the safety factor q at $\hat{\rho} = 0$ and $\hat{\rho} = 0.95$ for the simulations of scenario A done with RAPTOR (continuous line) and ASTRA (dashed line). The beginning of the flat top is highlighted.

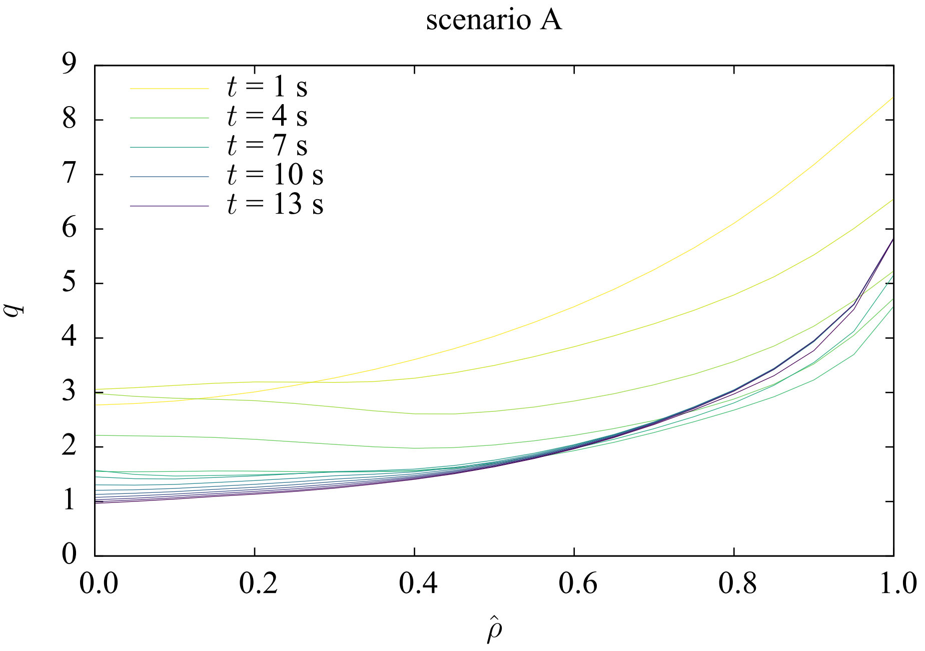

Figure 3.8: Radial profile of the safety factor at different instants during the simulation of the scenario A obtained with RAPTOR.

accordance, we can see that the q_0 computed by RAPTOR overestimates the one computed by ASTRA. The reason, that will be more evident in the scenario E simulation, is that the value of q near the core undergoes a distension with a characteristic time of the order of a couple of seconds before settling at its final value, probably due to effects caused by a small difference in core resistivity. This behaviour is more evident in figure 3.8, where we can see the radial profiles of q calculated by RAPTOR at different times during the discharge. As can be seen, the profiles stabilize rather quickly after the beginning of FT for values of $\hat{\rho} > 0.5$ but change more slowly near the core. Generally, given the rapidity of this process and the length of the FT, this behaviour is not cause of concern. Since q_0 remains above unity, no sawteeth have been triggered during the simulation.

3.2 Simulation of scenario E and comparison with the results obtained with METIS

3.2.1 Scenario E description and inputs

Scenario E represents an advanced phase in DTT operations where it will reach its full capabilities, with the full suite of external heating systems and able to test all the divertor configurations. The reference SN scenario has a plasma current $I_p = 5.5\,\mathrm{MA}$, a $B_0 = 5.96\,\mathrm{T}$, $q_{95} = 2.89$, $k_{95} = 1.65$, $\delta_{95} = 0.33$ and $\beta_p = 0.65$ although the simulated run has different q_{95} [CGM+24].

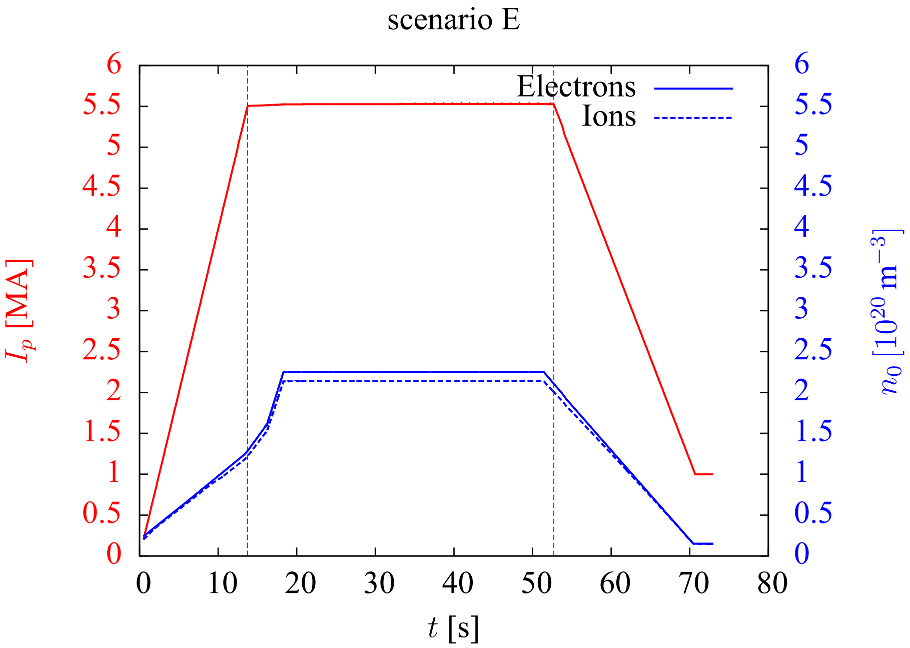

Figure 3.9: Plasma current and particle density at $\hat{\rho} = 0$ for ions and electrons used by METIS. These values (along with the full radially dependant density profile) have been used as inputs for RAPTOR. Both the beginning and end of the flat top are highlighted.

Like for scenario A, RAPTOR will solve the equations for T_e, T_i and ψ. In this case the simulation will involve a full discharge, with ramp up, flat top and ramp down (RD), lasting a total of 73 s with FT going from 13.75 to 52.7 s. The plasma current is raised to a value of 5.53 MA during RU and remains stable before decreasing linearly during RD down to a value of 1 MA 3 s before the end of the discharge. The density profiles are taken as inputs from the METIS simulation, with both their value at the plasma center and the value of plasma current being shown in figure 3.9. Two density profiles used as input are shown in figure 3.10, one during the RU before H-mode activation and the other during FT in H-mode. The on-axis toroidal magnetic field has been imposed as $B_0 = 5.85$ T for the whole discharge. The parameters of the Bohm-gyroBohm model chosen are $\alpha_{Be} = 3 \cdot 10^{-5}$, $\alpha_{Bi} = 3 \cdot 10^{-5}$, $\alpha_{gBe} = 1 \cdot 10^{-2}$ and $\alpha_{gBi} = 1.75 \cdot 10^{-2}$. The deposition profile of the heating systems is more complex, with ECRH injecting 29 MW during FT mostly at $\hat{\rho} = 0.2$, NBI injecting 10 MW at the plasma center and the ICRH injecting up to 6 MW at $\hat{\rho}$ mostly between 0.2 and 0.6. The total power injected and deposition depths of the external heating systems is shown in figure 3.11. The H-mode is activated between $t = 12.505$ s and $t = 53.903$ s with transport barrier at $\hat{\rho}_{\text{ped}} = 0.95$. The time grid has been built with variable time steps of 0.1 s for $t < 16$ s and $t > 53$ s, 0.01 for $16\,\text{s} < t < 21\,\text{s}$, 0.02 s for $21\,\text{s} < t < 25$ s and 0.03 s for $25\,\text{s} < t < 53$ s, a choice made through trial and error to improve convergence times while keeping the computational load as low as possible. All the other settings are equivalent to those used in the case of the scenario A.

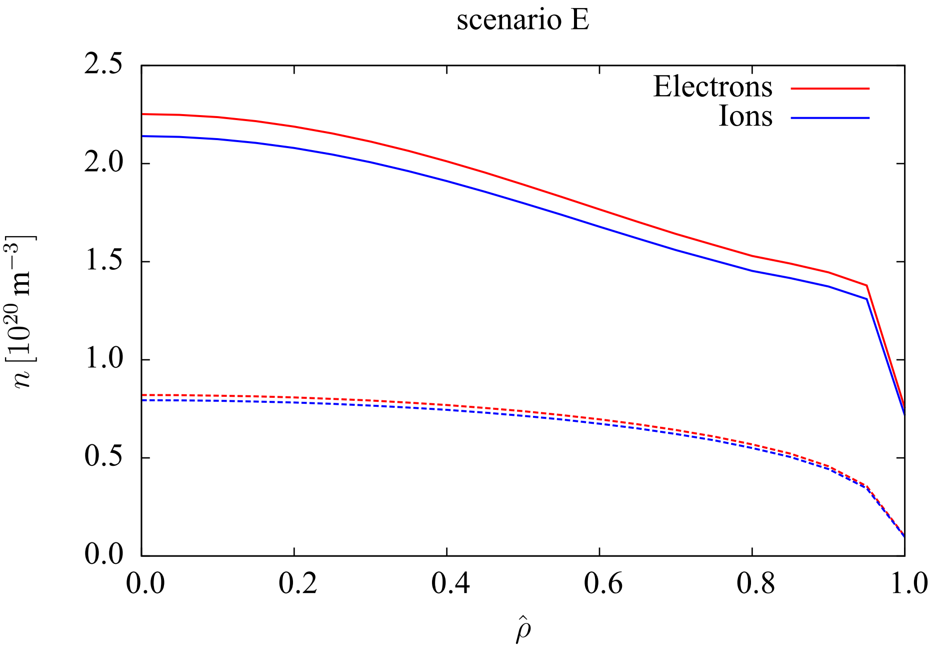

Figure 3.10: Ions and electrons numerical density profiles in function of $\hat{\rho}$ at $t = 8.00$ s (dashed line) and at $t = 30.01$ s (continuous line) used by METIS and given as input to RAPTOR. Both these profiles are the results of a linear interpolation between two pairs of instants in the METIS time grid, between $t = 7.9515$ s and $t = 8.3655$ s for the dashed line and between $t = 29.8922$ s and $t = 30.3062$ s for the continuous line.

3.2.2 The METIS modelling tool

METIS is a fast plasma transport simulator designed for faster-than-real-time results written in MATLAB, C and FORTRAN. Its description is taken from [Art+18].

It contains a full 2-D equilibrium solver that periodically updates the parameters of the flux surfaces that are then used to solve the flux transport equation with all its terms. METIS uses a neoclassical current diffusion model and computes the poloidal flux on a mesh of equidistant radial points. To speed up the calculations the flux surfaces are parameterized based on only their Shafranov shift, ellipticity and triangularity. Additionally a full spacial description of the LCFS can be provided that in turn is used to continually morph the moment description of the other flux surfaces.

METIS simplifies heat transport by using a 0D-1D model that decouples the temporal and spatial evolution of temperature profiles. The first step consists in computing the time derivative of the internal energy with a parameterization of power losses and by obtaining the energy confinement time via several possible scaling laws. Both scaling laws for L and H-mode are provided, as well as mixed laws for intermediate regimes. The global energy equation is then used to re-normalize the heat conductivity coefficients that in turn are used to calculate the temperature profiles using steady-state transport equations for diffusive transport only. Alternatively,

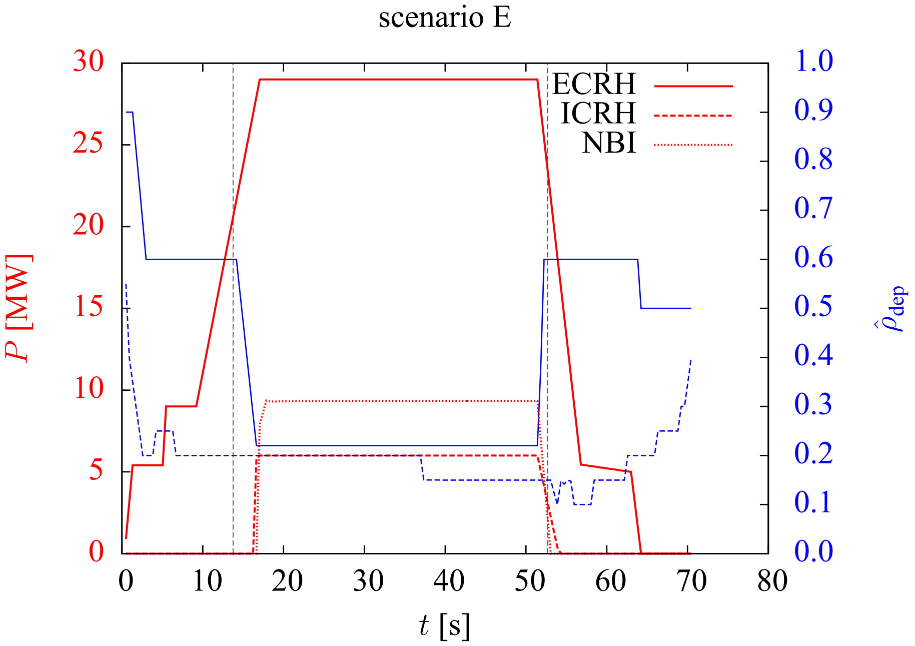

Figure 3.11: Total power injected by the external heating systems (red) in function of time for the scenario E simulation. The maximum of deposition for the ECRH and ICRH is also shown (blue). Both the beginning and end of the flat top are highlighted.

purely conductive equations can be used. The way this is done is to first compute the relative profile of the electron diffusion coefficient using several possible models (including a Bohm-gyroBohm model). Then the ion coefficient profile is taken as a re-scaling of the electron one. Finally their absolute values are chosen so that the energy integral is consistent with the total thermal energy previously calculated. In H-mode the top of the pedestal is used as boundary condition.

The electron density is computed based on the average line density, the peaking factor (ratio between density on the magnetic axis and average density) and the density at the separatrix. A fixed equation for the profile dependent on this values is given for L-mode while a cubic Hermite polynomial interpolation is performed in H-mode with the additional constraints of a flat profile at the center, a monotonically decreasing temperature and a prescribed density at the top of the pedestal. The profiles of electron and ion temperature and ion density can also be recalculated via a post processing with a neural network such as Qualikiz-NN. The density of most other species is then computed based on the user prescribed plasma composition and line average effective charge of the plasma. Their profile is a re-scaling of the electron density profile. Additionally, METIS utilizes special treatments for helium ashes (in the case of a D-T plasma) and tungsten impurities.

METIS is also capable of modelling the plasma rotations with a simplified model suited for mostly NBI driven rotation. It works in an analogous way to the heat calculation: first the time derivative of the total momentum is computed by taking into account momentum sources from NBI, RF driven rotation, parallel electric fields, intrinsic sources and friction on neutrals. Then the plasma edge momentum is calculated assuming it is purely convective and that there is no friction with the scrape-off layer. Finally, using these results, the radial profile of rotation is found assuming it is homothetic to one of the kinetic profiles (usually ion temperature), and from it the radial electric field can be calculated.

Various modules are included in METIS to compute the source terms in the current diffusion and heat transport equations. Sources can either be externally prescribed as radial time-dependent profiles or calculated based on the plasma characteristics. Among the implemented sources there are external heating systems, fusion reactions of thermal ions, pellets, radiative processes, ripple effects and so on.

3.2.3 Results

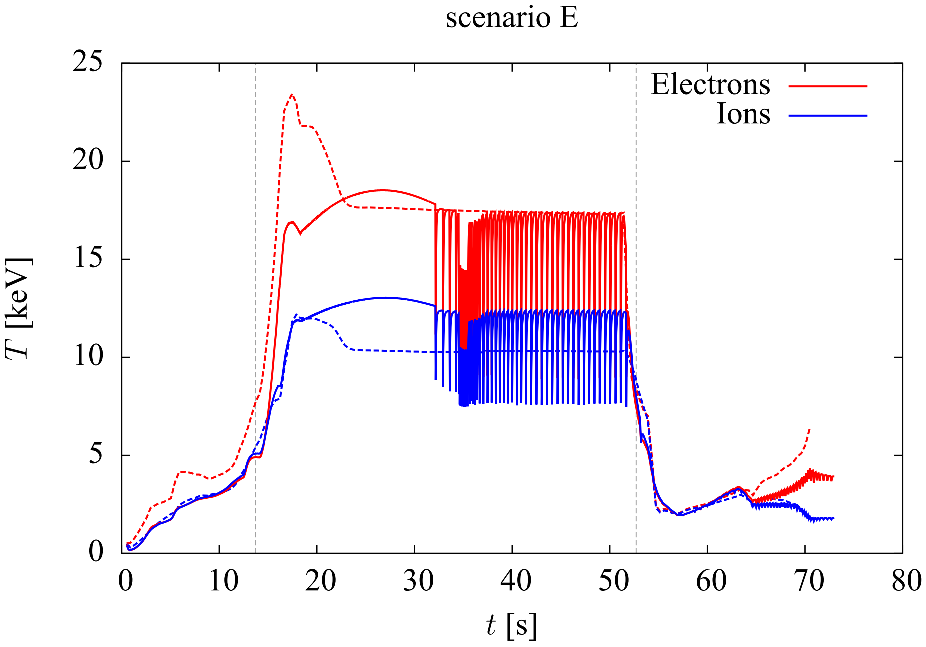

Figure 3.12: Ions and electrons temperature at $\hat{\rho} = 0$ for the simulations of scenario E done with RAPTOR (continuous line) and METIS (dashed line). Both the beginning and end of the flat top are highlighted.

Similarly to the previous scenario, we obtained good results when compared to METIS. In figure 3.12 we can see the core temperature behaviour. In this case, roughly 20 seconds after FT we have the onset of sawtooth crashes, with variations of the temperature of the order of 5 keV and frequencies of the order of 2 Hz. Contrary to the scenario A simulation, in this case the electron temperature relaxes to a value close to that of METIS but the ion temperature

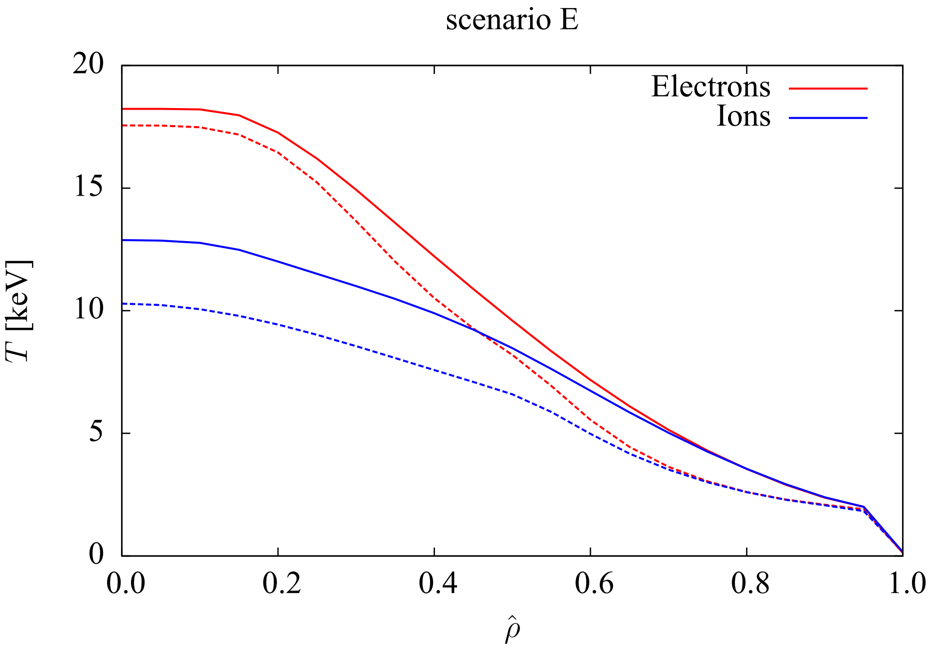

Figure 3.13: Ions and electrons temperature profiles in function of $\hat{\rho}$ at $t = 30.01$ s for the simulations of scenario E done with RAPTOR (continuous line) and METIS (dashed line).

is overestimated by more than 2 keV. A sample profile taken at $t = 30.01$ s is shown in figure 3.13. In this case the shape of the profile is similar except for its derivative near the plasma edge, causing the overestimation near the core. The relative difference computed with equation (3.1) is shown in figure 3.14. While during RU and RD the difference swings from 10% to 50%, during FT we have $\sigma_T \sim 10\%$ for electrons and $\sim 25\%$ for ions. The spikes of higher σ_T correspond to sampling of the profiles during a sawtooth crash. It is worth noting that METIS doesn't model actual crashes with the corresponding shape change of the various profiles and instead employs a brute force approach by imposing $q_0 = 1$ when the conditions for the presence of sawteeth are met. The difference in core temperature might be attributed to the simplified method used by METIS to compute the temperature profiles compared to the full resolution of the transport equations performed by RAPTOR.

We can clearly see this in figure 3.15, where the q_0 time evolution is shown. In this case, while in METIS it goes to one and it's kept constant during the FT, in RAPTOR there is a relaxation phase similar to that seen in the scenario A lasting for more than 10 s, before a quick drop and the onset of sawteeth. From that point onward the value of q_0 periodically goes below unity until the crash is triggered and brings it again to one. In the same figure the value of q_{95} is also shown and, like with scenario A, it's in good accordance with the reference. Both the frequency and magnitude of the sawteeth in the RAPTOR simulation are in accordance with other studies performed on the scenario E of DTT [CGM+24] using the sophisticated integrated suite of codes JINTRAC [Rom+14].

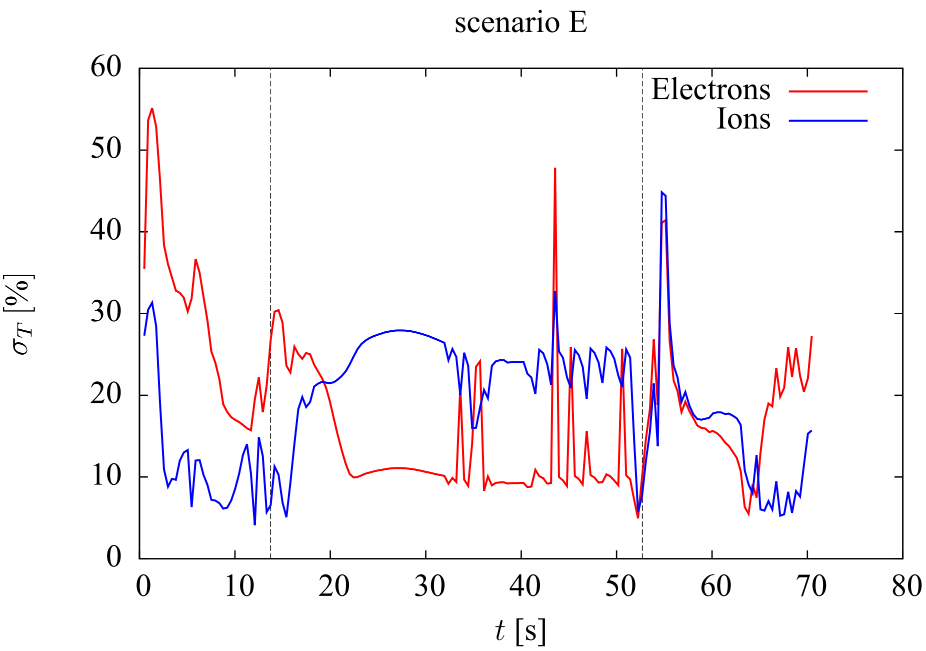

Figure 3.14: Normalized standard deviation between the temperatures computed by RAPTOR and METIS in the simulation of the scenario E. The beginning and end of the flat top are highlighted.

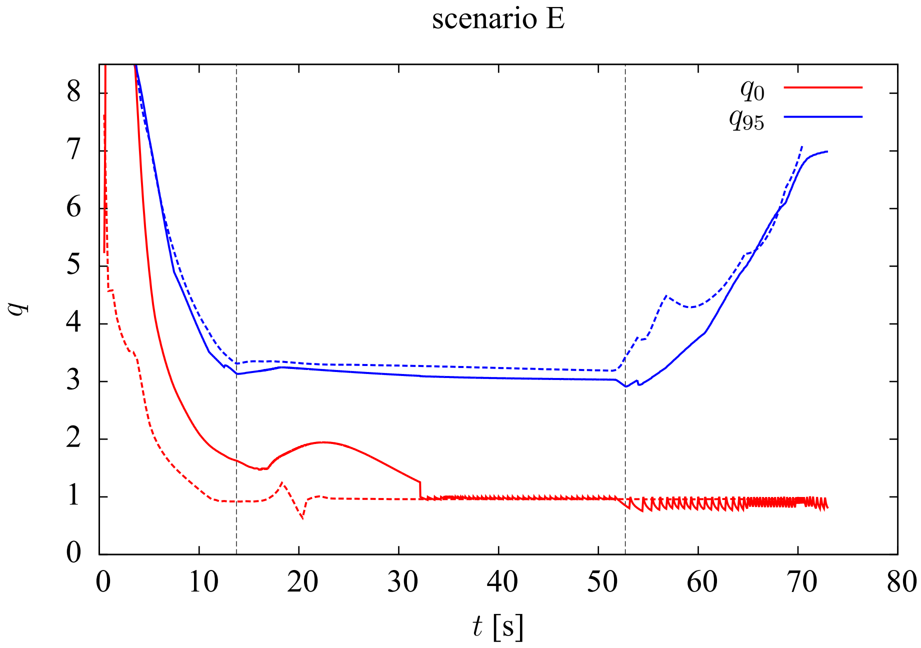

Figure 3.15: Values of the safety factor q at $\hat{\rho} = 0$ and $\hat{\rho} = 0.95$ for the simulations of scenario E done with RAPTOR (continuous line) and METIS (dashed line). Both the beginning and end of the flat top are highlighted.

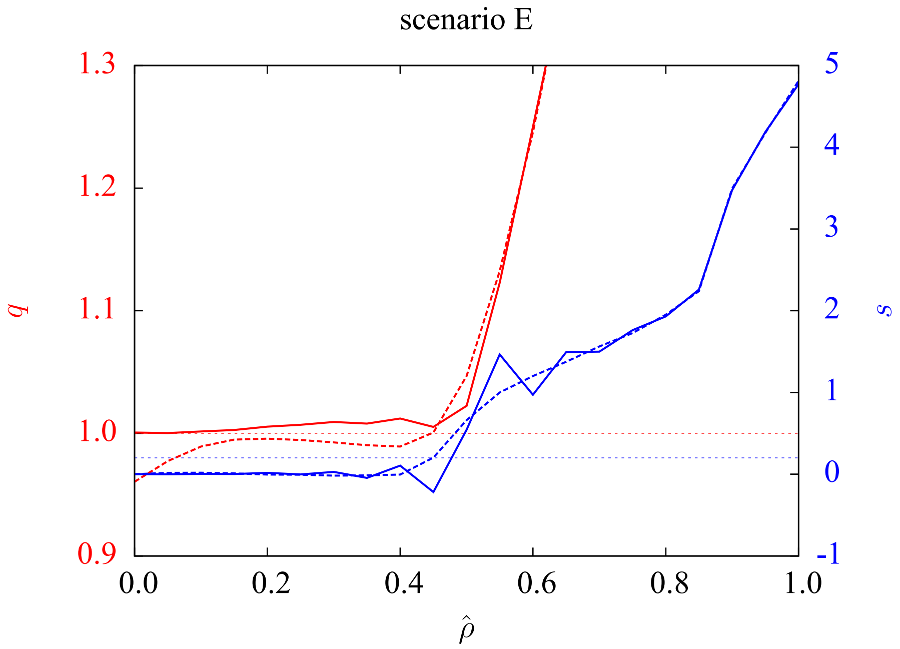

Figure 3.16: Radial profiles of the safety factor q and the magnetic shear s at $t_1 = 41.38$ s (dashed line) and at $t_2 = 41.41$ s (solid line) from the simulations of scenario E done with RAPTOR. A sawtooth crash has been triggered between the two instants. The horizontal line serve to highlight the $q = 1$ surface (red) and $s = 0.2$ point (blue).

We will now focus on the effect of a sawtooth crash on the profiles. We will consider two subsequent time steps during FT, the first at $t_1 = 41.38$ s and the second at $t_2 = 41.41$ s with a sawtooth being triggered between them. In figure 3.16 we can see the comparison between the q profiles and the shear before and after the crash. At t_1 we have q_0 below unity and $q = 1$ at $\hat{\rho} =\sim 0.45$ with the corresponding shear going above 0.2. This triggers the crash forcing q_0 to return above one. The temperature profiles are shown in figure 3.17. The crash causes an expulsion of hot plasma from the core and a sharp increase in temperature at $\hat{\rho} = 0.45$ before the profile returns to its normal shape for $\hat{\rho} > 0.6$. At $\hat{\rho} \sim 0.35$ we can see that the temperatures before and after the crash are roughly the same. This position is called *inversion radius* and it's an important parameter to characterize the sawtooth behavior.

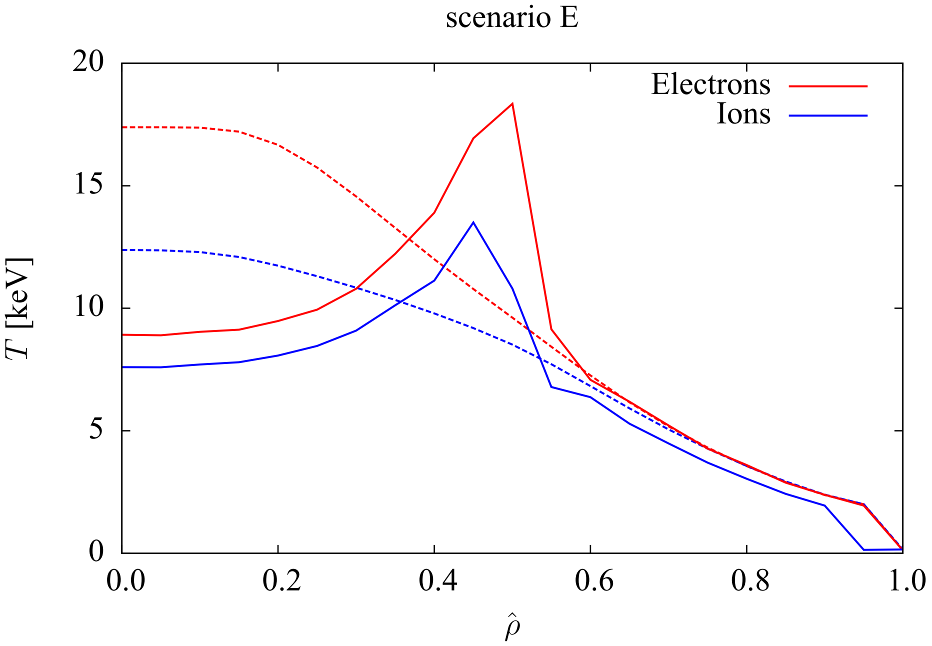

Figure 3.17: Radial profiles of the temperature of ions and electrons at $t_1 = 41.38$ s (dashed line) and at $t_2 = 41.41$ s (solid line) from the simulations of scenario E done with RAPTOR. A sawtooth crash has been triggered between the two instants.

Chapter 4

Sawtooth control

4.1 Double sweeping test

In this chapter, we document the ability of RAPTOR to accurately model the physical behaviour of the DTT system for what concerns the phenomenon of sawtooth crashes. It has been experimentally shown that the sawtooth period is highly sensitive to heating injection near the $q = 1$ surface, with a substantial stabilization caused by the reduction of the magnetic shear in that point [Han+91]. On top of providing a mean of control of the sawtooth crashes, this phenomenon can be experimentally exploited to provide useful information on the q profile: the strategy is to modify the deposition depth of one of the heating systems while monitoring the period of the sawteeth τ_{sw}, with the depth at which it reaches a maximum corresponding to the position of the $q = 1$ surface that can thus be practically identified. This kind of measurements takes the name of **sweeping experiment** [Pie+99]. The HCD system of choice is the ECRH given its narrow deposition profile.

A synthetic sweeping experiment has thus been performed by modifying the scenario E simulation with a substitution of the deposition profiles of the ECRH and ICRH systems with equivalent gaussian profiles, maintaining the same total power and distribution width. During the first and last portion of the simulation the position of the deposition peak $\hat{\rho}_{\text{dep}}$ is the nominal one used up until now while, after a suitable amount of time from the beginning of FT, as to allow the q profile stabilize, the $\hat{\rho}_{\text{dep}}$ of the ECRH system as been varied in a sweep and the evolution of the sawtooth frequency recorded. The sweeping time is 20 s, with sweeping start at $t = 32$ s and end at $t = 52$ s, just before the start of RD. The deposition depth has been varied from $\hat{\rho}_{\text{dep}} = 0.2$ to $\hat{\rho}_{\text{dep}} = 0.8$ with constant increments at each time step. It's worth pointing out that usually the sweeping is experimentally performed not by acting on the heating system and changing the heating profile, but instead by varying the toroidal magnetic field since it's what determines the deposition depth of the ECRH system [Pie+99]. Opposite to this, in our simulation B_T is kept constant and the profile changed. To verify the presence of hysteresis

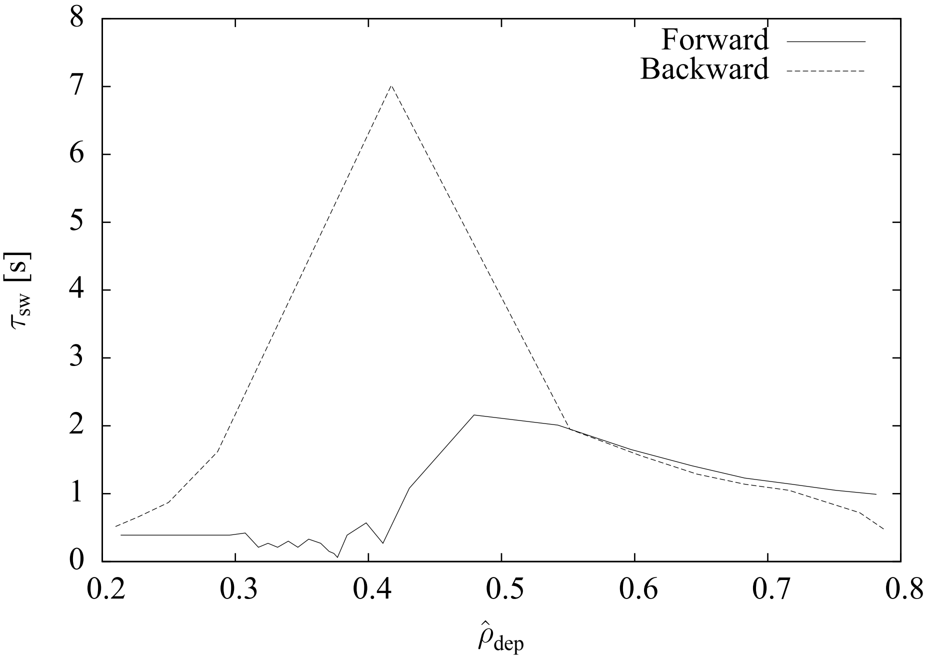

Figure 4.1: Sawtooth sweeping test performed on the scenario E by modifying the radial deposition depth of the ECRH system. The sawtooth period is shown for two tests, one performed by moving varying $\hat{\rho}_{\text{dep}}$ from 0.2 to 0.8 and the other vice-versa.

effects, two tests have been performed, the first with $\hat{\rho}_{\text{dep}}$ moving outward from the center of the plasma and the second with it moving inward from its edge.

The resulting sawtooth periods are shown in figure 4.1. The period is simply taken as the time difference between subsequent crashes, with the associated position as the deposition position at halfway time between the two sawteeth. The forward sweep has a maximum period of 2.34 s at $\hat{\rho} = 0.4985$. For values of $\hat{\rho} < 0.4$ the period is below 0.5 s given that the deposition of power inside the $q = 1$ surface has a destabilizing effect on sawteeth. Once the deposition depth gets closer to $q = 1$ the period rapidly increases before decreasing towards values of ~ 1 s for higher values of $\hat{\rho}$. For the reverse sweep instead the periods are much longer, with a peak at $\hat{\rho} = 0.3984$ and $\tau_{\text{sw}} = 7.32$ s. There is therefore a substantial difference in both position and period of these maxima that can be explained by different means. There is experimental evidence of hysteresis effects in these kind of sweeping experiments [Pal+09]. The reason is that deposition inside or outside the $q = 1$ surface respectively peaks or broadens the current profile, increasing the radius of the $q = 1$ surface in the first case or shrinking it in the second, reproducing what we found in our test. To prove that this is the case, in figure 4.2 is shown the current density profiles of the forward and reverse sweep near the moments of maximum sawtooth period. The difference in period can instead being explained by the fact that in our test we are moving the whole ECRH profile that provides most of the external heating causing, in the case of the reverse sweep where it's suddenly displaced at the edge of the plasma, a significant

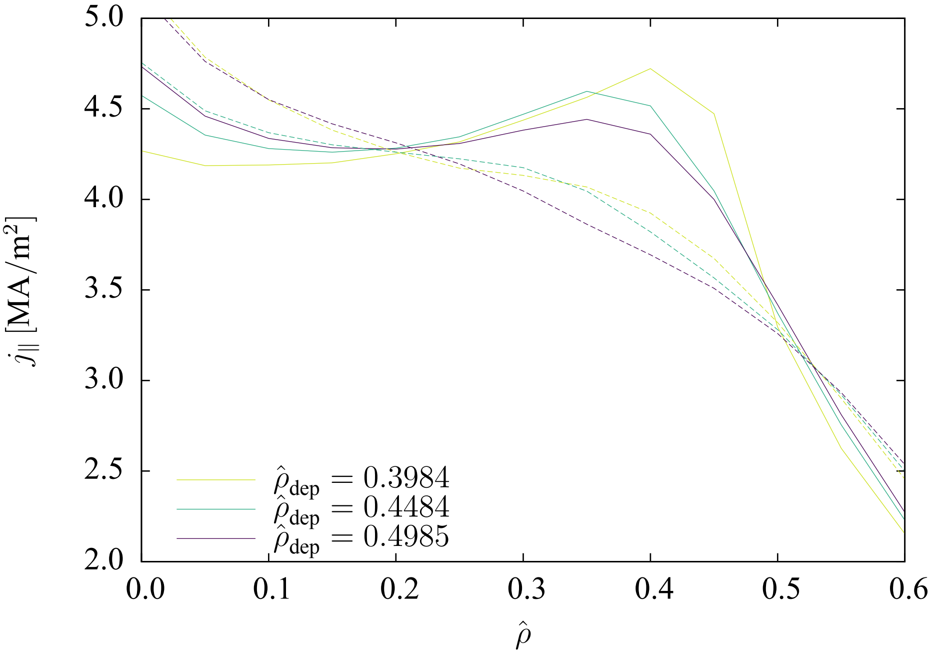

Figure 4.2: Radial profiles of parallel current density for the forward (solid line) and backward (dashed line) sweeping test. In both cases three profiles are shown, corresponding to the moments when we had the maximum sawtooth period in the forward and backward sweep and the average between the two.

drop of the core temperature. This in turns has a stabilizing effect on sawteeth. The two possible positions of the $q = 1$ surface are subject to uncertainties due to the period sampling rate being of the order of the frequency of the sawtooth and due to this hysteresis effect. A crude estimation of the value we are searching for could be obtained by a simple average of what we obtained with the forward and backward sweep, lending $\hat{\rho}_{q=1} = 0.4484$.

To verify the accuracy of this value, a series of simulations have been performed with the deposition depth being changed from one to the other in steps, within a range including the point of maximum of the forward sweeping and that of the reverse sweeping. In all cases the deposition has been kept fixed at the various $\hat{\rho}_{\text{dep}}$ between $t = 32$ s and $t = 52$ s. An example of the resulting temperature evolution is shown in figure 4.3 where in this case the deposition depth is slightly larger than the maximum obtained with the forward sweep. The results for all the tested values of $\hat{\rho}_{\text{dep}}$ are shown in figure 4.4, where each point is an average taking into considerations only the periods after the sawteeth stabilized following the change in $\hat{\rho}_{\text{dep}}$, thus excluding the first crashes. The maximum is at $\hat{\rho}_{q=1} = 0.452$ with $\tau_{\text{sw}} = 4.16$. This is notably very close to the average of the forward and reverse sweep, with a small relative difference of $\Delta\hat{\rho} = 0.0036$, i.e. less than 0.4% of the total radius. This confirms that the estimation of the deposition depth at which we have maximum τ_{sw} is accurate. Now we want to check if it actually

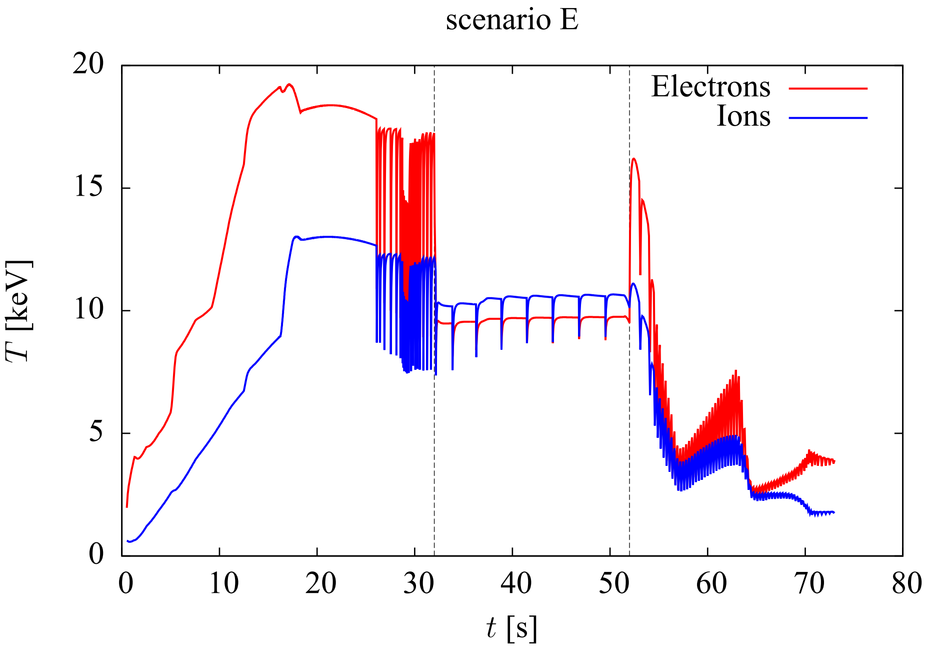

Figure 4.3: Example of stabilization of sawteeth using the ECRH. The graph shows the core temperature evolution of a simulation of the scenario E, with the difference that between $t = 32$ s and $t = 52$ s (marked by dashed black lines), the deposition depth has been changed to $\hat{\rho}_{\text{dep}} = 0.5320$.

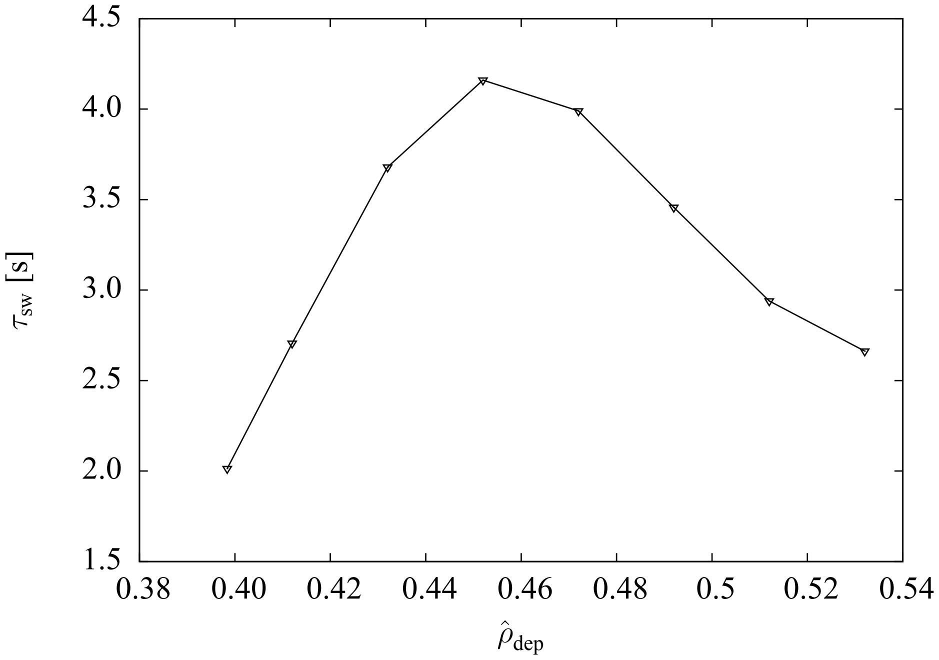

Figure 4.4: Sawtooth period in function of $\hat{\rho}_{\text{dep}}$ for simulations of the scenario E. The deposition depth has been maintained at that specific values between $t = 32$ s and $t = 52$ s. The periods are averages that consider only crashes happening after the sawtooth regime stabilized.

corresponds to the $q = 1$ surface.

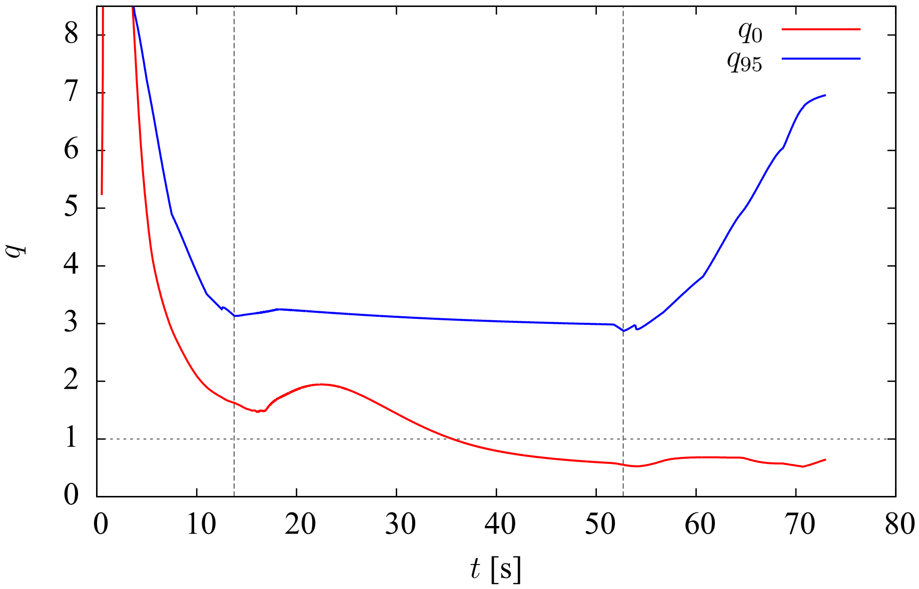

Figure 4.5: Values of the safety factor q at $\hat{\rho} = 0$ and $\hat{\rho} = 0.95$ for the simulations of scenario E done without sawtooth module. Both the beginning and end of the flat top are highlighted as well as the value $q = 1$.

In order to obtain a qualitative value of the position of the $q = 1$ surface another simulation of scenario E has been performed without activating the sawtooth crash module. This way the q profile was allowed to relax and the $q = 1$ surface entered the plasma. The evolution of the resulting q_0 and q_{95} is shown in figure 4.5. While the q_{95} values are similar to those obtained with sawteeth, q_0 goes below unity and continues to relax to lower values up to the end of the FT. In order to find the position at which we have $q = 1$ it was assumed that the q profiled was linear between the last point of the radial mesh with $q < 1$ and the first with $q > 1$ and the value of $\hat{\rho}_{q=1}$ computed through a simple proportion. The results are shown in figure 4.6. In this simulation the $q = 1$ surface enters the plasma at $t = 35.62$ s and quickly moves to $\hat{\rho}_{q=1} = 0.4231$. It then slowly relaxes outward, reaching $\hat{\rho}_{q=1} = 0.4576$ at the end of FT. While our estimations fall inside this range and are relatively close to the end value of the position, $\hat{\rho}_{q=1}$ appears to be changing up to the end of FT and because of this we cannot be sure that it has reached a final equilibrium value. Regardless, we can say that our estimation for the position of the $q = 1$ surface is accurate when considering the timescales of the simulation.

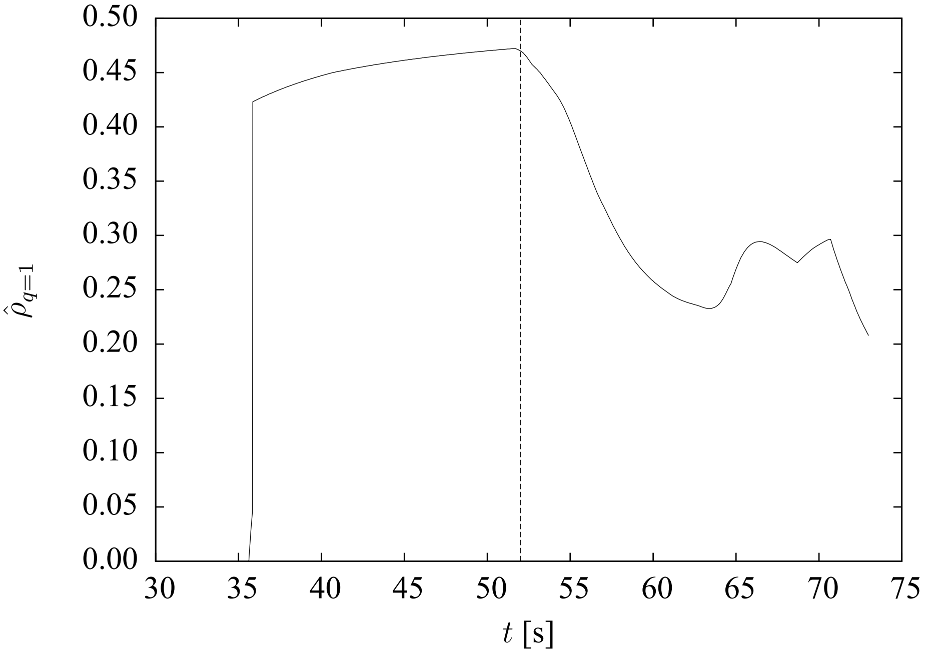

Figure 4.6: Evolution of the $q = 1$ surface position over time. The results come from a simulation of the scenario E where the sawtooth module has been deactivated. The end of FT is highlighted.

4.2 Effects of sweeping time

A further useful test is to verify the dependency of the simulation results on the sweeping time Δt_{sw}. Ideally, we would want to minimize it in order to optimize the experimental time, while still retaining a sufficient radial resolution and accuracy. A series of 5 simulations based on scenario E have been performed, each with a sweeping of the ECRH going from $\hat{\rho}_{\text{dep}} = 0.2$ to $\hat{\rho}_{\text{dep}} = 0.8$. Each sweeping starts at $t = 32$ s but with varying end times, ranging from $t = 46$ s to $t = 52$ s. This way each sweep will have the same starting condition but different duration, from $\Delta t_{\text{sw}} = 14$ s to $\Delta t_{\text{sw}} = 20$ s. The results with the sawteeth periods in function of $\hat{\rho}_{\text{dep}}$ are shown in figure 4.7. Moreover, to better quantify the results and reduce the effects of the sampling time of the frequencies, a gaussian fit has been performed on the peaks of each set of data, excluding the data points with shorter periods for depositions near the core and the tail with longer periods after the peak for larger $\hat{\rho}_{\text{dep}}$. The fitting function is

$$t_{\text{sw}} = A \exp\left[-\left(\frac{\hat{\rho}_{\text{dep}} - \mu_{\text{dep}}}{\sigma_{\text{dep}}}\right)^2\right]$$

It should be noted that the values of μ_{dep} do not correspond to the actual position of the $q = 1$ surface due to the skew of the period profiles and are only indicatively used to verify the presence

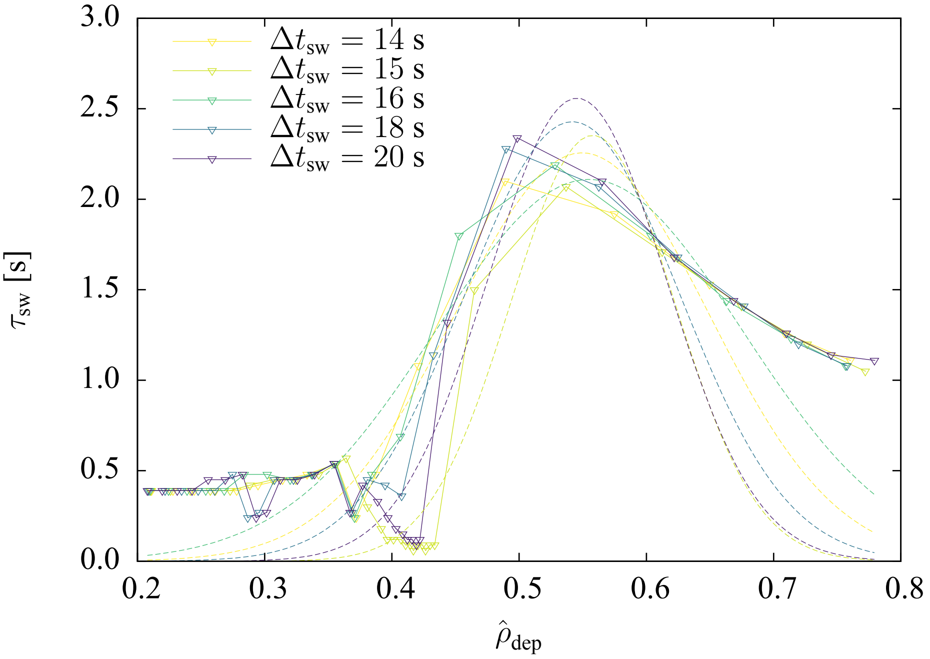

Figure 4.7: Sweeping tests performed with different possible sweeping times. The sawtooth period is shown in function of the deposition depth. All the tests have been performed with equal initial time $t = 32$ s and varying end time. Gaussian fits of each peak are also shown (dashed lines).

of any significant change in the results. The results of this fits are listed in table 4.1 while the resulting fitting function are also superimposed to the data in figure 4.7. In particular the position of the peak of the gaussian have good compatibility between each other and demonstrate how the sweeping test could in theory be performed with shorter periods without loss of accuracy.

$\Delta t_{\rm sw}$ [s]	A [s]	$\mu_{\rm dep}$	$\sigma_{\rm dep}$
14	2.3 ± 0.2	0.55 ± 0.01	0.14 ± 0.02
15	2.3 ± 0.4	0.56 ± 0.01	0.09 ± 0.02
16	2.1 ± 0.2	0.55 ± 0.01	0.17 ± 0.02
18	2.4 ± 0.3	0.54 ± 0.01	0.12 ± 0.02
20	2.6 ± 0.5	0.54 ± 0.01	0.10 ± 0.02

Table 4.1: Results of gaussian fits on the sawtooth frequency in function of deposition depth for the sweeping test with variable duration.

Chapter 5

Conclusions

The Divertor Tokamak Test facility (DTT) facility will provide invaluable scientific and engineering knowledge on design and operations of tokamak divertors in regimes of interest for the future DEMO experiment and the following commercial nuclear fusion reactors. In order to provide adequate real-time feedback control to DTT, it's necessary to simulate the complex behaviour of tokamak plasma with all the relevant physics while at the same time using a lean enough code able to operate faster-than-real-time. The strategy is to consider an axisymmetric model of the plasma lying on nested magnetic field flux surfaces, separating the problem in the calculation of the shape of these surfaces and of the evolution of one dimensional, radially dependent profiles of quantities of interest considered constant over them. In this work we concentrated on the second part of the problem, using a rapid, control-oriented, plasma transport simulator code called **RAPTOR** [Fel+18b] in order to validate its future use in the control loop of DTT.

We simulated the evolution of the plasma temperature and current profiles of DTT in two possible operation scenarios:

- **Scenario A**, corresponding to first operations of DTT, with reduced plasma current $I_p = 2\,\mathrm{MA}$ and magnetic field $B_0 = 3$ and with only one of the three types of external heating systems.
- **Scenario E**, corresponding to a fully operational DTT with $I_p = 5.5\,\mathrm{MA}$ and $B_0 = 5.96$ and equipped with a complete suite of external heaters. Our simulation in particular was the first modelling of this scenario using RAPTOR.

Our results were meant to reproduce two previous modelling of DTT obtained with other transport codes as a way to test the accuracy of RAPTOR, therefore the same inputs and parameters of those simulations have been used when setting up ours. The scenario A simulation was compared with one obtained with ASTRA [PY02], a highly customizable, physics-oriented plasma transport code more computationally intensive than RAPTOR. Our results during the plasma steady state (i.e. the portion of the plasma discharge when feedback control is expected to be used) had only a 10% temperature mean deviation compared to ASTRA and we obtained an extremely good accordance also in the profile of the safety factor q. The scenario E simulation was instead compared with one obtained with METIS [Art+18], another fast transport simulator code that achieves faster-than-real-time performance at the expense of considerable model simplifications. In this case we still obtained a 10% mean deviation in the electron temperature but we found a large discrepancy in the ion temperature that is overestimated by 30%. Despite this, the overall shape of the temperature profiles is in good accordance as are the values of the q profile. In the case of the scenario E, RAPTOR was also able to model a particular kind of plasma instabilities called *sawtooth instabilities*, caused by the onset of a kink instability on the $q = 1$ plasma surface and linked to the expulsion of hot particles from the plasma core and a flattening of the q profile. While METIS is not able to fully model these instabilities, our results are compatible with other simulations of the scenario E performed with the considerably more computationally demanding code JINTRAC [CGM+24][Rom+14], despite the simplified sawtooth module used by RAPTOR.

To further validate the ability of reproduce the physical behaviour of tokamak plasma, the scenario E simulation was modified to perform a simulated *sawtooth sweeping* experiment. These kind of experiments are usually performed in actual machines to study the safety factor profile, and in particular the position of the $q = 1$ surface, by varying the deposition position of the external heating systems while monitoring the period of sawteeth. Two trials have been performed, with the power deposition point moving from the interior of the plasma to the edge and vice-versa, finding an experimentally expected hysteresis effect. The accuracy of our estimation of the $q = 1$ surface was confirmed with a series of simulations to study the sawteeth behavior with power deposition depth kept constant, rather than constantly moving like in the sweeping experiment, and a simulation without sawteeth crashes to estimate the position of the surface in a way that would otherwise be impossible in a real life experiment. Moreover, a series of experiments with varying sweep duration have been performed to verify that the sweeping speed doesn't significantly influences the final results.

Despite the results obtained, further work will be needed before RAPTOR can be effectively integrated in the DTT control system. In particular:

- In our simulations RAPTOR didn't model some aspects of the physics of DTT, more specifically the presence and effects of impurities in the plasma. The next step in DTT simulations might be the inclusion of a suitable impurity simulation model.
- Both our simulation considered a specific magnetic configuration called Single-Null, most commonly used in modern tokamaks. However, since DTT will be a testbed for several alternatives configurations, RAPTOR should ideally be able to accurately simulate them. Therefore, further studies in this direction are advisable.

- The RAPTOR transport model could still be optimized to obtain even better accordance with the reference simulations, either by a further fine tuning of its model parameters or by substituting the Bohm-gyroBohm transport model we used with more advanced alternatives like the QLKNN-4Dkin model already implemented in RAPTOR.

In conclusion, RAPTOR has proved its ability to accurately simulate the DTT experiment in different conditions and regimes. It has for the first time successfully modelled a fully operational version of DTT, while also reproducing important physical effects in accordance both with other reference simulations and expected experimental behaviours, confirming its value as rapid and flexible modelling tool. While further optimizations and test will have to be performed, RAPTOR has substantially moved forward in its path to became an integral part of the DTT control system.

Bibliography

[AAM15] R. Albanese, R. Ambrosino, and M. Mattei. “CREATE-NL+: A robust control-oriented free boundary dynamic plasma equilibrium solver”. In: *Fusion Engineering and Design* 96-97 (2015). Proceedings of the 28th Symposium On Fusion Technology (SOFT-28), pp. 664–667. issn: 0920-3796.

[Amb+08] G. Ambrosino et al. “Plasma Strike-Point Sweeping on JET Tokamak With the eXtreme Shape Controller”. In: *Plasma Science, IEEE Transactions on* 36 (July 2008), pp. 834 –840.

[Art+18] J.F. Artaud et al. “Metis: a fast integrated tokamak modelling tool for scenario design”. In: *Nuclear Fusion* 58.10 (Aug. 2018), p. 105001.

[CGM+24] F. Crisanti, G. Giruzzi, P. Martin, et al. *Divertor Tokamak Test facility Research Plan Version 1.0*. ENEA, 2024.

[Cha10] I T Chapman. “Controlling sawtooth oscillations in tokamak plasmas”. In: *Plasma Physics and Controlled Fusion* 53.1 (Nov. 2010), p. 013001.

[DTT] *DTT press gallery*. Available at `https://www.dtt-project.it/index.php?option=com_content&view=article&id=842&Itemid=1918`. Accessed 2024/06/26.

[Erb+98] M. Erba et al. “Validation of a new mixed Bohm/gyro-Bohm model for electron and ion heat transport against the ITER, Tore Supra and START database discharges”. In: *Nuclear Fusion* 38.7 (July 1998), p. 1013.

[Fed+01] Gianfranco Federici et al. “Plasma-material interactions in current tokamaks and their implications for next step fusion reactors”. In: *Nuclear Fusion* 41.12 (2001), p. 1967.

[Fel11] Federico Felici. “Real-Time Control of Tokamak Plasmas: from Control of Physics to Physics-Based Control”. In: (2011), p. 293.

[Fel+18a] F. Felici et al. “Real-Time multichannel tokamak plasma profile simulations using the RAPTOR code and the QLKNN first-principle transport model”. English. In: *45th EPS Conference on Plasma Physics, EPS 2018*. Ed. by S. Coda et al. 45th European Physical Society Conference on Plasma Physics (EPS 2018), EPS 2018 ; Conference date: 02-07-2018 Through 06-07-2018. European Physical Society (EPS), 2018, pp. 1256–1259.

[Fel+18b] F. Felici et al. “Real-time-capable prediction of temperature and density profiles in a tokamak using RAPTOR and a first-principle-based transport model”. In: *Nuclear Fusion* 58.9 (July 2018), p. 096006.

[Han+91] K. Hanada et al. “Sawtooth stabilization by localized electron cyclotron heating in a tokamak plasma”. In: *Phys. Rev. Lett.* 66 (15 Apr. 1991), pp. 1974–1977.

[HH76] F. L. Hinton and R. D. Hazeltine. “Theory of plasma transport in toroidal confinement systems”. In: *Rev. Mod. Phys.* 48 (2 Apr. 1976), pp. 239–308.

[IAEA02] Vienna International Atomic Energy Agency. *ITER Technical Basis*. ITER EDA Documentation Series n. 24, Jan. 2002.

[IPEG99] ITER Physics Expert Group on Confinement, Transport, et al. “Chapter 2: Plasma confinement and transport”. In: *Nuclear Fusion* 39.12 (Dec. 1999), p. 2175.

[ITER] *ITER project newsline*. Available at `https://www.iter.org/newsline/-/2567`. Accessed 2024/06/26.

[Kad75] B B Kadomtsev. “Disruptive instability in tokamaks”. In: *Sov. Tech. Phys. Lett. (Engl. Transl.); (United States)* 1:5 (Jan. 1975).

[Law57] J D Lawson. “Some Criteria for a Power Producing Thermonuclear Reactor”. In: *Proceedings of the Physical Society. Section B* 70.1 (Jan. 1957), p. 6.

[LBS96] H. Lütjens, A. Bondeson, and O. Sauter. “The CHEASE code for toroidal MHD equilibria”. In: *Computer Physics Communications* 97.3 (1996), pp. 219–260. issn: 0010-4655.

[Li+14] Shunjie Li et al. “Optimal Tracking for a Divergent-Type Parabolic PDE System in Current Profile Control”. In: *Abstract and Applied Analysis* (June 2014), pp. 1–8.

[Mar+19] Raffaele Martone et al. *Divertor Tokamak Test facility – Interim Design Report*. ENEA Frascati Research Center, Apr. 2019. isbn: 978-88-8286-378-4.

[Pal+09] J I Paley et al. “Real time control of the sawtooth period using EC launchers”. In: *Plasma Physics and Controlled Fusion* 51.5 (Mar. 2009), p. 055010.

[PBR96] F Porcelli, D Boucher, and M N Rosenbluth. “Model for the sawtooth period and amplitude”. In: *Plasma Physics and Controlled Fusion* 38.12 (Dec. 1996), p. 2163.

[Pie+99] Z.A. Pietrzyk et al. “Behaviour of central plasma relaxation oscillations during localized electron cyclotron heating on the TCV tokamak”. In: *Nuclear Fusion* 39.5 (May 1999), p. 587.

[PY02] Gregorij V Pereverzev and PN Yushmanov. *ASTRA. Automated system for transport analysis in a tokamak*. Rep. Max-Planck-Institut für Plasmaphysik, 2002.

[Rom+14] Michele Romanelli et al. “JINTRAC: A System of Codes for Integrated Simulation of Tokamak Scenarios”. In: *Plasma and Fusion Research* 9 (2014), pp. 3403023–3403023.

[Wes11] John Wesson. *Tokamaks; 3rd ed.* International series of monographs on physics. Oxford: Oxford Univ. Press, 2011.

Acronyms

CiC Cable-in-Conduit.
CS Central Solenoid.

DN Double-Null.
DTT Divertor Tokamak Test facility.

ECE Electron Cyclotron Emission.
ECRH Electron Cyclotron Resonance Heating.
ELM Edge Localized Mode.

FT Flat Top.

HCD Heating Current Drive.

ICRH Ion Cyclotron Resonance Heating.

LCFS Last Closed Flux Surface.
LH Lower Hybrid Resonance Heating.

MHD Magnetohydrodynamics.

NBI Neutral Beam Injector.
NIR Near Infrared.
NT Negative Triangularity.
NTM Neoclassical Tearing Mode.

PCS Porous Capillary System.
PF Poloidal Field.
PID Proportional-Integral-Derivative.
PWI Plasma-Wall Interaction.

RD Ramp Down.
RU Ramp Up.
RWM Resistive Wall Modes.

SFD Snowflake Divertor.
SN Single-Null.
SOL Scrape Off Layer.
SXD Super-X Divertor.

TF Toroidal Field.
TOF Time Of Flight.

XD X-divertor.
XSC eXtreme Shape Control.